Technische
Universität
München

Fakultät
für
Physik

Walther-Meissner-
Institut für Tief-
temperaturforschung

Master Thesis
Abschlussarbeit im Masterstudiengang Physik

Spin Hall magnetoresistance in antiferromagnetic NiO and α-Fe_2O_3

Johanna Fischer

Garching, 31. August 2017

Erstgutachter (Themensteller): Prof. Dr. Rudolf Gross
Zweitgutachter: Prof. Dr. Christian Pfleiderer
Advisor: Dr. Matthias Opel, Dr. Stephan Geprägs

Contents

Chapter 1

Introduction

Spintronic devices integrating ferromagnetic materials and normal metals in multilayer hybrid structures represent well established basic elements in the field of data storage. For *future* spintronic applications, *anti*ferromagnetic (AF) materials have come into the focus of interest [1–11]. They promise to increase the dynamics [12] as well as the robustness against external magnetic field perturbations [10, 13, 14]. Recently, the spin Hall effect [15–18], the spin-Seebeck and the spin-Nernst effects [19–23], and other spin transport phenomena [24–30] were reported in different AF insulators. For the application of such materials in data storage devices, however, a robust detection scheme for their AF magnetization state is desired. The spin Hall magnetoresistance (SMR) effect [31] could represent a sensitive probe for the readout of the AF magnetization – so simple that only a planar metallic Hall bar electrode has to be implemented in a bilayer thin film system.

The SMR originates from the interplay of charge and spin currents between a magnetic insulator with magnetization $\mathbf{M}$ and a non-magnetic metal, exhibiting a spin Hall effect (SHE) [32] and a finite spin polarization $\mathbf{s}$ at the interface. This gives rise to an exchange of spin-angular-momentum between $\mathbf{M}$ and $\mathbf{s}$ and manifests itself in a characteristic dependence of the resistivity on the angle $\sphericalangle(\mathbf{M}, \mathbf{s})$ [33]. The effect was first experimentally reported in $Y_3Fe_5O_{12}$(YIG)|Pt hybrid structures [31] and theoretically explained by a non equilibrium proximity effect [33]. The validity of the SMR model has been confirmed for YIG|Pt [31, 34–39] and other collinear ferromagnetic insulator|normal metal systems like YIG|Ta [36], Fe_3O_4|Pt [34], $NiFe_2O_4$|Pt [34], and $CoFe_2O_4$|Pt [40]. Recently, the SMR was used to resolve the spin structure residing on non-collinear magnetic sublattices in canted ($Gd_3Fe_5O_{12}$) [41] or spiral ferrimagnets (Cu_2OSeO_3) [42]. Furthermore the SMR was found in FM|antiferromagnet (AFM)|Pt hybrid structures like YIG|NiO|Pt [30, 43–

45] and in AFM|Pt samples [46, 47]. As the SMR requires only a simple planar metallic electrode on top of the AFM, this discovery makes it a promising tool for future applications.

In this thesis, we systematically study the SMR effect in antiferromagnetic nickel oxide (NiO)|platinum (Pt) and hematite (α-Fe_2O_3)|platinum (Pt) bilayers and find a 90° shift of the SMR signal in angle-dependent magnetoresistance (ADMR) measurements with respect to the SMR using collinear ferromagnetic insulators like YIG. Our results demonstrate that the SMR effect reflects the spin structure of the AF sublattices in the AFM. We furthermore observe a strong dependence of the SMR amplitude on the magnetic field magnitude in the NiO|Pt heterostructures. To explain this behaviour in the framework of the SMR theory, we develop an antiferromagnetic multidomain model and take into account magnetic field induced modifications of the three-domain state.

To give a brief introduction of the SMR we start with the theoretical background in Chapter 2. Chapter 3 introduces a theoretical model for a three-domain AFM with a high magnetostriction and derives the expected SMR signal. In Chapters 4 and 5 the experimental data, using NiO|Pt and Fe_2O_3|Pt heterostructures for SMR measurements, are shown together with the material properties of the AFM NiO and Fe_2O_3. The summary and the outlook are given in Chapter 6 to conclude this thesis.

Chapter 2

Theoretical Background

We first give a brief introduction to charge and spin currents. Second, we present the spin Hall effect and the inverse spin Hall effect (SHE and ISHE) that are necessary to understand the principle of the spin Hall magnetoresistance (SMR) effect. As in our experiments we investigated antiferromagnetic insulators (AFI) we focus on the differences of the SMR there, compared to the ferrimagnetic insulators (FMI), that have multiply been presented in literature so far [31, 34–42].

2.1 Charge and spin currents

A charge current in a normal metal (e.g. Pt, Cu) consists of moving electrons. For this charge current, the electrons' second degree of freedom, their spin angular momentum, is not relevant. We now consider a two-spin channel model. Electrons with spin states "up" and "down" contribute equally to the charge current

$$\mathbf{J}_q = \mathbf{J}_\uparrow + \mathbf{J}_\downarrow \tag{2.1}$$

(see Fig. 2.1 (a)). In contrast their spin direction changes the sign of their contribution to the spin current

$$\mathbf{J}_s = -\frac{\hbar}{2e}\left(\mathbf{J}_\uparrow - \mathbf{J}_\downarrow\right) \ . \tag{2.2}$$

Here, e is the elementary charge and $\hbar$ is the reduced Planck constant. For a pure charge current, the equal contributions result in $\mathbf{J}_s = 0$ (Fig. 2.1(a)). For ferromagnetic metals (e.g. Fe), the densities of states at the Fermi level are unequal for the two spin directions. Therefore, the two spin states are not equally occupied.

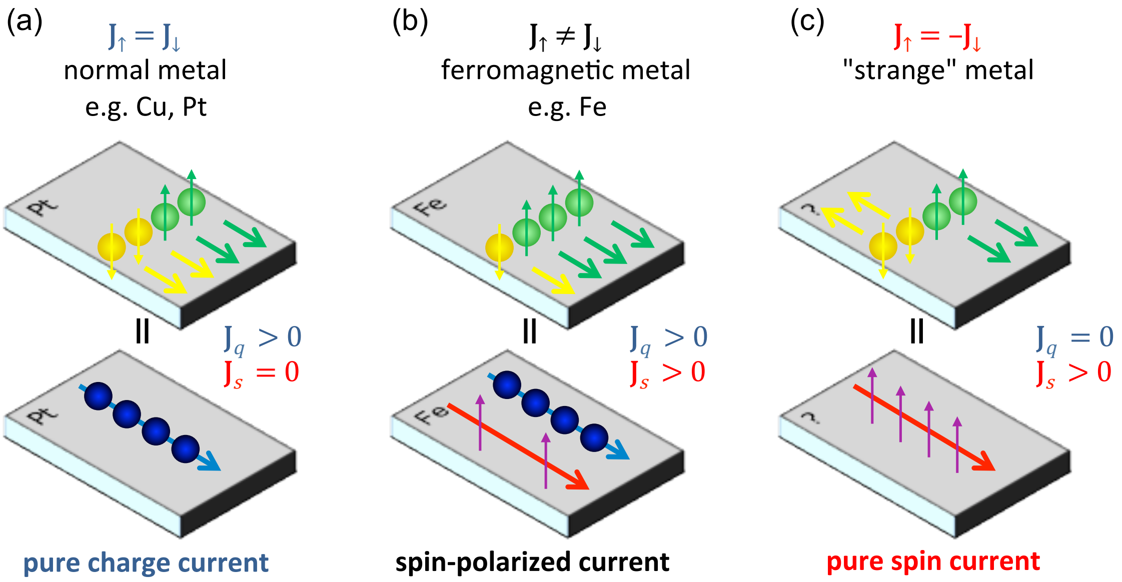

Figure 2.1: (a) Schematic illustration of a pure charge current $\mathbf{J}_q$ with the same number of spin "up" and spin "down" electrons moving in the same direction, no spin current $\mathbf{J}_s$. (b) Unequal amount of spin "up" and spin "down" electrons moving in the same direction lead to finite $\mathbf{J}_q$ and $\mathbf{J}_s$. (c) Realization of a pure spin current $\mathbf{J}_s$ without $\mathbf{J}_q$ for electrons with opposite spin moving in opposite directions.

This does not affect $\mathbf{J}_q > 0$, but leads to a finite $\mathbf{J}_s > 0$ and a so called spin-polarized current (see Fig. 2.1 (b)). If we imagine a "strange" metal, where the electrons with different spin states move in opposite directions (Fig. 2.1 (c)), the result would be the inverse: A pure spin current $\mathbf{J}_s > 0$ with zero charge current $\mathbf{J}_q = 0$.

2.2 Spin Hall effect and inverse spin Hall effect

To create a spin current from a charge current one can make use of the spin Hall effect (SHE) [32]. There, due to spin-dependent scattering effects originating from spin orbit interactions, a charge current causes a spin current

$$\mathbf{J}_s = \alpha_{\mathrm{SH}}(-\frac{\hbar}{2e})\mathbf{J}_q \times \mathbf{s} \tag{2.3}$$

(Fig. 2.2 (a)). The efficiency of this effect is given by the material specific spin Hall angle α_{SH}. A non toxic material with a sufficiently high $\alpha_{\mathrm{SH}}= 0.11$ is Pt [34].

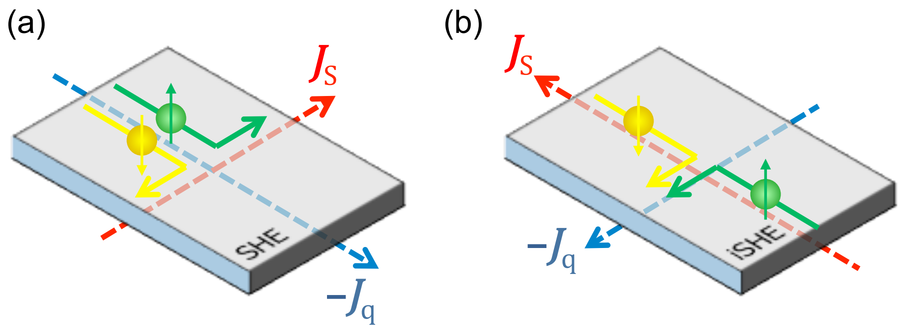

Figure 2.2: Illustration of the (a) spin Hall effect (SHE) and the (b) inverse spin Hall effect (ISHE). $\mathbf{J}_q$ and $\mathbf{J}_s$ denote the charge and the spin current, respectively.

The inverse spin Hall effect (ISHE) converts a spin current back to a charge current, see Fig. 2.2 (b). The direction of the generated current is always perpendicular to both the direction of the initial current and the spin direction $\mathbf{s}$.

2.3 Spin Hall magnetoresistance

The spin Hall magnetoresistance (SMR) effect emerges at the interface between a normal metal (NM) and a magnetic insulator (MI) [31]. Via the SHE a finite spin current is generated in the NM resulting in a spin accumulation at the interface to the MI. Depending on the direction of its sublattice magnetizations $\mathbf{M}$ this spin accumulation can relax in the MI via spin transfer torque [33]. For maximum relaxation, the spin direction $\mathbf{s}$ has to be perpendicular to $\mathbf{M}$ (Fig. 2.3 (a)). In the parallel configuration, however, the spin current is reflected at the interface and retransformed via ISHE to a charge current (Fig. 2.3 (b)).

The difference between relaxation and reflection of $\mathbf{J}_s$ manifests itself in different electrical resistances ρ_{long} or ρ_{trans} of the NM, measured along $-\mathbf{J}_q$ or perpendicular to $-\mathbf{J}_q$, respectively. This effect is used in our experiments where we manipulate the magnetic sublattices with an external magnetic field and detect the related resitivity changes. Using a ferrimagnet (FM) as MI permits to reorient $\mathbf{M}$ with an external field $\mathbf{H}$. The sublattices align (anti)parallel to $\mathbf{H}$ for sufficiently high magnitudes of the external field. To define the direction of $\mathbf{H}$, we introduce the angle α between $-\mathbf{J}_q$ and $\mathbf{H}$. So, $\alpha = 0°$ ($\mathbf{h}\|\mathbf{j}$) corresponds to the case of relaxation of the spin current and, therefore, a higher resistivity ρ_{long} than for $\alpha = 90°$ ($\mathbf{H}\|\mathbf{t}$), where the

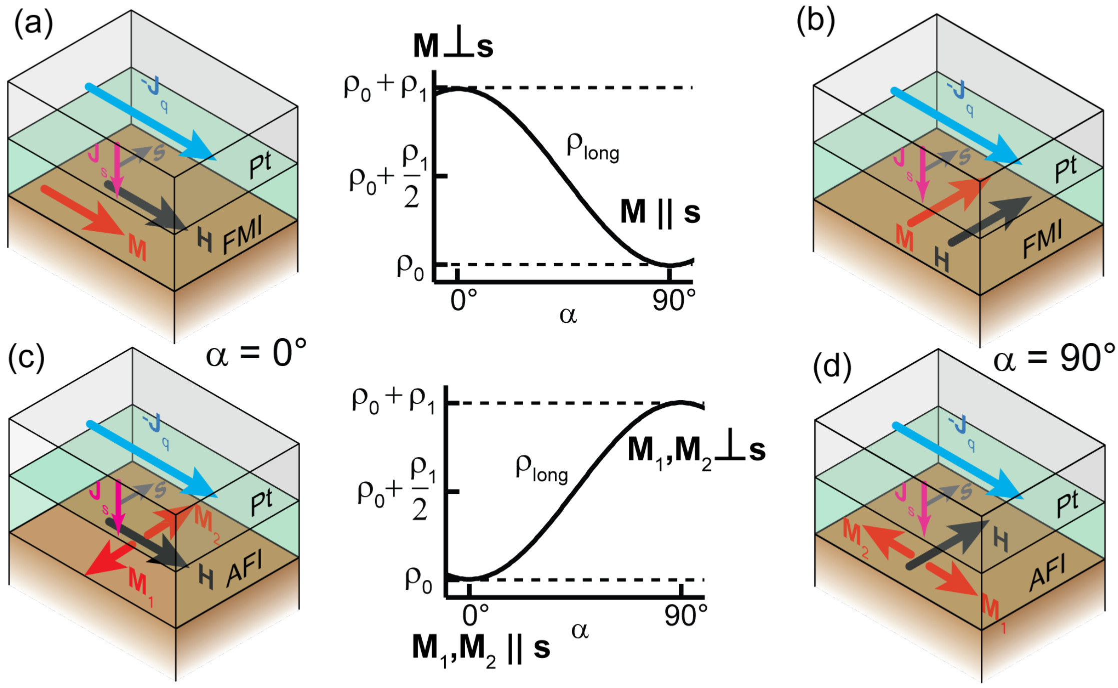

Figure 2.3: Via the SHE a charge current $\mathbf{J}_q$ is transformed to a spin current $\mathbf{J}_s$ with a spin polarization $\mathbf{s}$ at the Pt|MI interface (the MI is a FMI in (a) and (b), an AFI in (c) and (d)). For perpendicular orientation between the magnetization $\mathbf{M}$ in the FMI (a) or $\mathbf{M}_{1,2}$ in the AFI (d) to $\mathbf{s}$, spin transfer torque with spin relaxation is possible and causes a higher resistivity ρ_{long} (measured along $\mathbf{J}_q$) than for $\mathbf{M} \parallel \mathbf{s}$ (b), or $\mathbf{M}_{1,2} \parallel \mathbf{s}$ (c). ρ_0 is the resistivity of the bare Pt electrode and ρ_1 is the SMR amplitude [33].

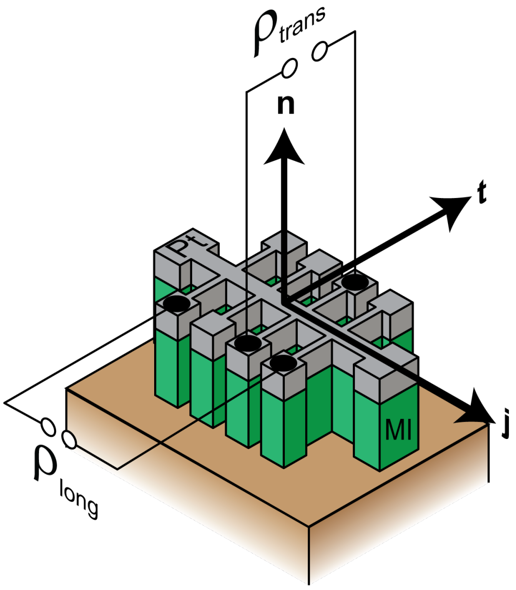

Figure 2.4: Measurement geometry of a metal insulator (MI)|Pt bilayer, patterned into a Hall bar structure via photolitography with current direction **j**, transverse axis **t** and normal direction **n**. ρ_{long} is determined along **j**, ρ_{trans} along **t** by measuring the voltage drop while applying a current along **j**.

spin current is retransformed to a charge current reducing the resistivity.

In this thesis, we focus on AFI as MI. We expect that their magnetic sublattices $\mathbf{M}_{1,2}$ orient perpendicular to **H** per magnetic domain [48, 49]. As shown in Fig. 2.3 (c,d) for a monodomain case, the relaxation and the reflection of $\mathbf{J}_s$ take place for different orientations of **H** from the FM case above. As a result, $\alpha = 0°$ corresponds now to the case of reflection with low ρ_{long} and $\alpha = 90°$ to the relaxation with high ρ_{long}.

In our measurements, we pattern the AFI|Pt bilayer into a Hall bar structure. This permits us to apply a current along the direction **j** ($\parallel -\mathbf{J}_q$) and measure a longitudinal resistivity (ρ_{long}) along **j** and a transverse resistivity (ρ_{trans}) along **t** (see Fig. 2.4). A rotation of **H** in the Hall bar plane is an "ip" rotation (Fig. 2.5(a)), in a plane perpendicular to **j** an "oopj" (Fig. 2.5(b)) and perpendicular to **t** an "oopt" rotation (Fig. 2.5(c)).

In the extended SMR theory, those longitudinal and transverse resistivities of the Pt layer are given by [33, 41]

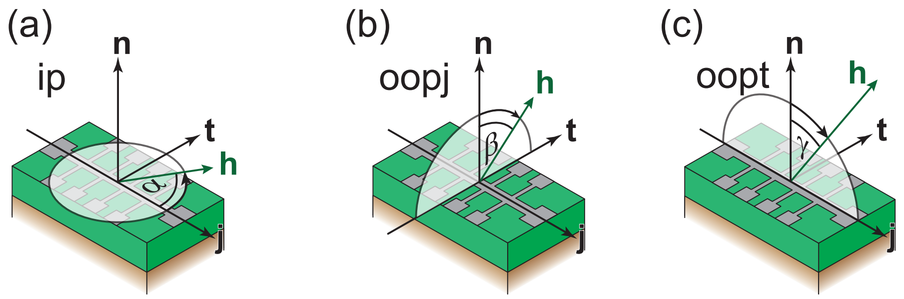

Figure 2.5: Definition of the rotation planes of the external magnetic field with unit vector **h**. (a) in the Hall bar plane (ip). (b) in a plane perpendicular to the current direction **j** (oopj). (c) in a plane perpendicular to the transvere direction **t** (oopt).

$$\rho_{\text{long}} = \rho_0 + \sum_X \rho_{1,X} \left[1 - (\mathbf{m}_X \cdot \mathbf{t})^2\right] \tag{2.4}$$

$$\rho_{\text{trans}} = \sum_X \rho_{3,X} \left[\mathbf{m}_X \cdot \mathbf{j}\right] \left[\mathbf{m}_X \cdot \mathbf{t}\right] \ , \tag{2.5}$$

where $\mathbf{m}_X$ are the unit vectors of the magnetizations of all sublattices X. ρ_0 is the resistivity of the bare Pt electrode, ρ_1 and ρ_3 are the maximal SMR amplitudes for the longitudinal and the transverse measurements, respectively [33]. We now define the angle between $\mathbf{m}_X$ and $\mathbf{j}$ as φ_X such that $\varphi_X = 0°$ means $\mathbf{m}_X \parallel \mathbf{j}$ and $\varphi_X = 90°$ means $\mathbf{m}_X \parallel \mathbf{t}$. Then $\mathbf{m}_X \cdot \mathbf{j} = \cos\varphi_X$ and $\mathbf{m}_X \cdot \mathbf{t} = \sin\varphi_X$.

In FMI, we only have one magnetic sublattice with magnetization $\mathbf{m}$ ($|\mathbf{m}| = 1$) oriented parallel to $\mathbf{H}$. So, $\varphi = \alpha$ and we get

$$\rho_{\text{long}} = \rho_0 + \rho_1[1 - \sin^2\alpha] = \rho_0 + \rho_1\cos^2\alpha = \rho_0 + \frac{\rho_1}{2} + \frac{\rho_1}{2}\cos 2\alpha \ , \tag{2.6}$$

$$\rho_{\text{trans}} = \rho_3 \sin\alpha\cos\alpha = \frac{\rho_3}{2}\sin 2\alpha \ . \tag{2.7}$$

For a single antiferromagnetic domain with two sublattices $X = 1, 2$ and no canting effects we assume $\mathbf{m}_1 = -\mathbf{m}_2 \perp \mathbf{H}$ ($|\mathbf{m}_1| = |\mathbf{m}_2| = 1$) [48, 49], resulting in $\varphi_1 = \alpha + 90°$

and $\varphi_2 = \alpha - 90°$. With $\rho_{1,1} = \rho_{1,2} = \rho_1/2$ and $\rho_{3,1} = \rho_{3,2} = \rho_3/2$ we obtain

$$\rho_{\text{long}} = \rho_0 + \rho_1[1 - \cos^2\alpha] = \rho_0 + \rho_1 \sin^2\alpha = \rho_0 + \frac{\rho_1}{2} - \frac{\rho_1}{2}\cos 2\alpha \ , \tag{2.8}$$

$$\rho_{\text{trans}} = \frac{\rho_3}{2}[(-\sin\alpha)\cos\alpha + \sin\alpha(-\cos\alpha)] = -\frac{\rho_3}{2}\sin 2\alpha \ . \tag{2.9}$$

In summary, the expected qualitative difference of the angle dependent magnetoresistance (ADMR) between the FMI and the AFI for an in-plane rotation of $\mathbf{H}$ is a 90° shift of the signal with respect to the angle α.

Chapter 3

Model for a three-domain AFM

We now present a model to calculate the SMR for a three-domain antiferromagnet under rotation in an external magnetic field $\mathbf{H}$. This configuration will be relevant for our experiments.

We consider a crystal structure with three distinguishable domains in an easy plane with an angle of 120° to each other (see Fig. 3.1(b)). Each antiferromagnetic domain D_k $(k = 1, 2, 3)$ consists of two magnetic sublattices, oriented in positive and negative sense along the staggered unit magnetization vectors $\mathbf{l}_k$ which are the normalized differences of the sublattice unit vectors $\mathbf{m}_{1,\mathrm{k}}$ and $\mathbf{m}_{2,\mathrm{k}}$ of the sublattice magnetizations, Fig. 3.1(a). For magnetotransport measurements we, furthermore, consider a metallic Hall bar on top of this AFM easy plane. The projections of $\mathbf{l}_k$ on the Hall bar directions $\mathbf{j}$ and $\mathbf{t}$ are defined as $l_j^{(k)} = \cos\varphi_k$ and $l_t^{(k)} = \sin\varphi_k$, with φ_k the angle between $\mathbf{l}_j^{(k)}$ and the current direction $\mathbf{j}$ (Fig. 3.1(c)). For the SMR calculation, we treat the interfaces between the Hall bar and the domains as serially connected resistors with mobile domain walls (blue in Fig. 3.1(b)) between them. The relative size (fraction) of each domain D_k is given by ξ_k. So the sum over all domains is $\sum_{k=1}^{3} \xi_\mathrm{k} = 1$. According to the SMR theory [15], the longitudinal and the transverse resistivities can be written as

$$\rho_\mathrm{long} = \rho_0 + \rho_1 \sum_{k=1}^{3} \xi_k [1 - (l_t^{(k)})^2] \ , \tag{3.1}$$

$$\rho_\mathrm{trans} = \rho_3 \sum_{k=1}^{3} \xi_{(k)} l_j^{(k)} l_t^{(k)} \ , \tag{3.2}$$

see also Eqs.(2.4) and (2.5). The angle between $\mathbf{H}$ and $\mathbf{j}$ is α and, therefore, the two components of the external field are given by $H_j = H\cos\alpha$ and $H_t = H\sin\alpha$. We

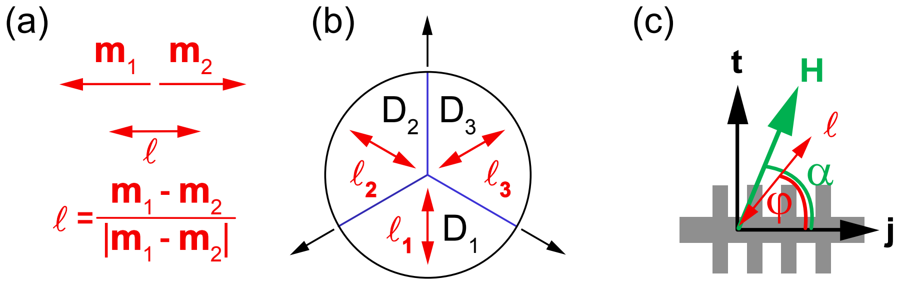

Figure 3.1: (a) Definition of the staggered magnetization vector $\mathbf{l}$ as the normalized difference of the unit vectors $\mathbf{m}_1$ and $\mathbf{m}_2$ of the sublattice magnetizations. (b) Illustration of the three-domain structure (D_1 - D_3). (c) Measurement geometry. The directions $\mathbf{j}$ and $\mathbf{t}$ are defined by the Hall bar (shaded area). α is the angle between the external magnetic field $\mathbf{H}$ and $\mathbf{j}$, φ is the angle between $\mathbf{l}$ and $\mathbf{j}$.

only consider external fields applied in the Hall bar plane.

In the following, we will first summarize the relevant microscopic forces on the magnetic sublattices to obtain the free energy of the system. Minimization of the free energy with respect to the domain fractions ξ_k and the directions of the sublattice magnetizations φ_k leads then to a field dependent microscopic domain picture and is used to calculate the SMR.

The following energy ansatz is adapted from a theoretical model Olena Gomonay proposed for the equilibrium domain structure in AFM in [46].

3.1 Relevant energies

In the absence of an external magnetic field $\mathbf{H}$, the magnetic structure is determined by the anisotropy energy

$$E_\mathrm{a} = \frac{1}{6} M V H_\mathrm{a} \langle \cos(6\varphi) \rangle \ , \tag{3.3}$$

leading to a six-fold anisotropy domain structure. $\langle ... \rangle$ is the mean average over the domain structure and defined as $\langle u \rangle = \sum \xi_k u^{(k)}$. M is the sublattice magnetization that is equal for all the antiferromagnetic moments in our model. V is the volume of the sample and H_a the magnetic anisotropy field. Since φ for each domain is defined with a 30° shift relative to the easy axes, E_a has a positive sign. For $\mathbf{H} \neq 0$, the six-fold anisotropic domain structure is influenced by two competing interactions, the Zeeman and the demagnetization energy. The Zeeman energy

$$E_\mathrm{Zee} = \frac{MVH^2}{2H_\mathrm{ex}} \langle \cos^2(\varphi - \alpha) \rangle - \frac{MVH^2}{4H_\mathrm{ex}} \tag{3.4}$$

defines the reorientation of $\mathbf{l}^{(k)}$ of the magnetic sublattices and creates an energetic difference between the before energetically degenerate domains. H_ex is the magnetic exchange field. This ansatz is taken from [50] where $E_\mathrm{Zee} \propto H^2, \cos^2 \sphericalangle(\mathbf{H}, \mathbf{l})$ and $E_\mathrm{a} \propto -\cos(6 \sphericalangle(\text{easy axis}, \mathbf{l}))$.

Furthermore, a (ponderomotive) force is generated and induces domain wall motion to eliminate energetically unfavourable domains. On the other hand, antiferromagnets with a pronounced magnetoelastic coupling show so-called destressing effects. The destressing energy

$$E_\mathrm{dest} = \frac{1}{2} H_\mathrm{dest} MV [\langle \cos 2\varphi \rangle^2 + \langle \sin 2\varphi \rangle^2] \tag{3.5}$$

favours a multidomain state and can be seen as an analogon to the demagnetization forces in ferromagnets [51–53]. H_dest is the magnetic destressing field and is given by the magnetostriction of the material. Domain wall motion is, however, limited by pinning effects like defects in the crystal, but in a first approximation we neglect this phenomenon [46]. The total energy

$$E_\mathrm{tot} = E_\mathrm{a} + E_\mathrm{Zee} + E_\mathrm{dest} \tag{3.6}$$

is the sum of E_a , E_Zee and E_dest. For the materials relevant in this thesis, the values for the anisotropy (H_a) and the exchange fields (H_ex) are of the order of 10 mT and 1000 T, respectively.

3.2 Minimization of the free energy

To calculate the magnetic domain structure we minimize the total energy with respect to the domain fraction ξ_k and the orientation of the staggered vectors $\mathbf{l}^{(k)}$ in each domain by setting $\frac{\partial E_\mathrm{tot}}{\partial \xi_k} = 0$ and $\frac{\partial E_\mathrm{tot}}{\partial \varphi_k} = 0$. We obtain three regimes dependent on the external magnetic field magnitude that have to be treated separately.

For high fields, the three domains become indistinguishible and for $H \geqslant H_{\mathrm{MD}}$ (H_{MD} is the monodomain field, see later) they behave as one large domain. For lower H, we separate between $H_{\mathrm{MD}}/\sqrt{2} \leq H < H_{\mathrm{MD}}$ where depending on the orientation of $\mathbf{H}$ two or three domains are existing, and $H < H_{\mathrm{MD}}/\sqrt{2}$ with an overall three-domain state.

3.2.1 Three-domain regime for $H < H_{\mathrm{MD}}/\sqrt{2}$

In the three-domain regime, we substitute $\xi_1 = 1 - \xi_2 - \xi_3$ and write all functions of ξ_k and φ_k using the aforementioned mean average over the domain structure. Differentiating the energies separately with respect to ξ_j and φ_j $(j = 2, 3)$ gives

$$\frac{\partial E_{\mathrm{a}}}{\partial \xi_j} = \frac{MVH_{\mathrm{a}}}{6}(\cos 6\varphi_j - \cos 6\varphi_1) \tag{3.7}$$

$$\frac{\partial E_{\mathrm{a}}}{\partial \varphi_j} = -MVH_{\mathrm{a}}\xi_j \sin 6\varphi_j \tag{3.8}$$

$$\frac{\partial E_{\mathrm{Zee}}}{\partial \xi_j} = -\frac{MVH^2}{2H_{\mathrm{ex}}}[\cos^2(\varphi_1 - \alpha) - \cos^2(\varphi_j - \alpha)] \tag{3.9}$$

$$\frac{\partial E_{\mathrm{Zee}}}{\partial \varphi_j} = -\frac{MVH^2}{2H_{\mathrm{ex}}}\xi_j \sin 2(\varphi_j - \alpha) \tag{3.10}$$

$$\frac{\partial E_{\mathrm{dest}}}{\partial \xi_j} = MVH_{\mathrm{dest}}[(\cos 2\varphi_j - \cos 2\varphi_1)\langle\cos 2\varphi\rangle + (\sin 2\varphi_j - \sin 2\varphi_1)\langle\sin 2\varphi\rangle] \tag{3.11}$$

$$\frac{\partial E_{\mathrm{dest}}}{\partial \varphi_j} = 2H_{\mathrm{dest}}MV\xi_j(\cos 2\varphi_j\langle\sin 2\varphi\rangle - \sin 2\varphi_j\langle\cos 2\varphi\rangle)\ , \tag{3.12}$$

and leads to

$$\frac{\partial E_{\mathrm{tot}}}{\partial \xi_j} = \frac{MVH_{\mathrm{a}}}{6}(\cos 6\varphi_j - \cos 6\varphi_1) - \frac{MVH^2}{2H_{\mathrm{ex}}}[\cos^2(\varphi_1 - \alpha) - \cos^2(\varphi_j - \alpha)] + \\ + MVH_{\mathrm{dest}}[(\cos 2\varphi_j - \cos 2\varphi_1)\langle\cos 2\varphi\rangle + (\sin 2\varphi_j - \sin 2\varphi_1)\langle\sin 2\varphi\rangle] = 0\ , \tag{3.13}$$

Since we are in the low-field regime, we consider the directions of the staggered magnetizations of the three domains as fixed and set $\varphi_1 = 270°$, $\varphi_2 = 150°$ and

$\varphi_3 = 30°$. With $j = 2, 3$, we obtain the following two equations

$$j = 2 \;\;\Rightarrow\;\; \frac{\sqrt{3}H^2}{4H_{\mathrm{ex}}}\sin(2\alpha + \frac{2\pi}{3}) + H_{\mathrm{dest}}[+\frac{3}{2}\langle\cos 2\varphi\rangle - \frac{\sqrt{3}}{2}\langle\sin 2\varphi\rangle] = 0 \tag{3.14}$$

$$j = 3 \;\;\Rightarrow\;\; \frac{\sqrt{3}H^2}{4H_{\mathrm{ex}}}\sin(2\alpha - \frac{2\pi}{3}) + H_{\mathrm{dest}}[-\frac{3}{2}\langle\cos 2\varphi\rangle - \frac{\sqrt{3}}{2}\langle\sin 2\varphi\rangle] = 0 \ . \tag{3.15}$$

We note that the contribution from the anisotropy energy cancels out. Summing and subtracting leads to

$$\langle\cos 2\varphi\rangle = -\frac{H^2\cos 2\alpha}{4H_{\mathrm{ex}}H_{\mathrm{dest}}} \tag{3.16}$$

$$\langle\sin 2\varphi\rangle = -\frac{H^2\sin 2\alpha}{4H_{\mathrm{ex}}H_{\mathrm{dest}}} \ . \tag{3.17}$$

Together with the definition of the mean average for

$$\langle\cos 2\varphi\rangle = \sum_{k=1}^{3}\xi_k\cos 2\varphi_k = \frac{3}{2}(\xi_2 + \xi_3) - 1 \tag{3.18}$$

$$\langle\sin 2\varphi\rangle = \sum_{k=1}^{3}\xi_k\sin 2\varphi_k = \frac{\sqrt{3}}{2}(\xi_3 - \xi_2) \ , \tag{3.19}$$

we obtain

$$\xi_2 = \frac{1}{3} - \frac{H^2}{4H_{\mathrm{ex}}H_{\mathrm{dest}}}(\frac{\cos 2\alpha}{3} - \frac{\sin 2\alpha}{\sqrt{3}}) \tag{3.20}$$

$$\xi_3 = \frac{1}{3} - \frac{H^2}{4H_{\mathrm{ex}}H_{\mathrm{dest}}}(\frac{\cos 2\alpha}{3} + \frac{\sin 2\alpha}{\sqrt{3}}) \tag{3.21}$$

$$\xi_1 = 1 - \xi_2 - \xi_3 = \frac{1}{3}(1 + \frac{2H^2\cos 2\alpha}{4H_{\mathrm{ex}}H_{\mathrm{dest}}}) \ . \tag{3.22}$$

For the two "extreme" directions of $\mathbf{H}$ ($\alpha = 0°$ and $\alpha = 90°$), this results in

$$\xi_{2,3}^{\alpha=0°} = \frac{1}{3}(1 - \frac{H^2}{4H_{\mathrm{ex}}H_{\mathrm{dest}}}) \tag{3.23}$$

$$\xi_{2,3}^{\alpha=90°} = \frac{1}{3}(1 + \frac{H^2}{4H_{\mathrm{ex}}H_{\mathrm{dest}}}) \tag{3.24}$$

$$\xi_{1}^{\alpha=0°} = \frac{1}{3}(1 + \frac{2H^2}{4H_{\mathrm{ex}}H_{\mathrm{dest}}}) \tag{3.25}$$

$$\xi_{1}^{\alpha=90°} = \frac{1}{3}(1 - \frac{2H^2}{4H_{\mathrm{ex}}H_{\mathrm{dest}}}) \; . \tag{3.26}$$

We see that for $\alpha = 0°$ the domain fractions ξ_2 and ξ_3 get zero at $H = H_{\mathrm{MD}} \equiv \sqrt{4H_{\mathrm{ex}}H_{\mathrm{dest}}}$. There the domains D_2 and D_3 disappear and only D_1 remains. We call H_{MD} the monodomain field. For $\alpha = 90°$, at $H = \frac{H_{\mathrm{MD}}}{\sqrt{2}}$, ξ_1 goes to zero and we obtain a two-domain state. In the next section, we will calculate the situation for the two remaining domains at fields $H_{\mathrm{MD}}/\sqrt{2} \le H < H_{\mathrm{MD}}$.

Now we calculate the resistivities ρ_{long} and ρ_{trans} using Eqs.(3.1) and (3.2) together with the values for ξ_2 and ξ_3 (Eqs. (3.20), (3.21)) and the angles $\varphi_1 = 270°$, $\varphi_2 = 150°$ and $\varphi_3 = 30°$. We obtain

$$\rho_{\mathrm{long}} = \rho_0 + \frac{\rho_1}{2} - \frac{\rho_1}{2}\frac{H^2}{H_{\mathrm{MD}}^2}\cos 2\alpha \; , \tag{3.27}$$

$$\rho_{\mathrm{trans}} = -\frac{\rho_3}{2}\frac{H^2}{H_{\mathrm{MD}}^2}\sin 2\alpha \tag{3.28}$$

and find a 180°-periodic oscillation of the resisitivities with an amplitude proportional to H^2.

3.2.2 Two-domain regime for $H_{\mathrm{MD}}/\sqrt{2} \le H < H_{\mathrm{MD}}$

From Eq.(3.26) we see that at $\alpha = 90°$ and $H_{\mathrm{MD}}/\sqrt{2} \le H < H_{\mathrm{MD}}$ we obtain a two-domain state. In this section, we are going to calculate ρ_{long} and ρ_{trans} for $H_{\mathrm{MD}}/\sqrt{2} \le H < H_{\mathrm{MD}}$ and angles α around $\alpha = 90°$ where only D_2 and D_3 are existing. [1]

Using $\xi_2 + \xi_3 = 1$ and minimizing the derivative $\frac{\partial E_{\mathrm{tot}}}{\partial \xi_2} = \frac{\partial E_{\mathrm{a}}}{\partial \xi_2} + \frac{\partial E_{\mathrm{Zee}}}{\partial \xi_2} + \frac{\partial E_{\mathrm{dest}}}{\partial \xi_2}$

---

[1] For a rotation of the external field starting from $\alpha = 90°$, at some critical angle depending on the external field magnitude D_1 reappears and the SMR follows Eq.(3.27).

with

$$\frac{\partial E_{\mathrm{a}}}{\partial \xi_2} = \frac{MVH_{\mathrm{a}}}{6}(\cos 6\varphi_2 - \cos 6\varphi_3) \tag{3.29}$$

$$\begin{aligned}\frac{\partial E_{\mathrm{Zee}}}{\partial \xi_2} &= -\frac{MVH^2}{2H_{\mathrm{ex}}}[\cos^2(\varphi_2-\alpha) - \cos^2(\varphi_3-\alpha)] \\ &= -\frac{MVH^2}{4H_{\mathrm{ex}}}[\cos 2\alpha(\cos 2\varphi_3 - \cos 2\varphi_2) + \sin 2\alpha(\sin 2\varphi_3 - \sin 2\varphi_2)] \end{aligned} \tag{3.30}$$

$$\frac{\partial E_{\mathrm{dest}}}{\partial \xi_2} = MVH_{\mathrm{dest}}[(\cos 2\varphi_2 - \cos 2\varphi_3)\langle\cos 2\varphi\rangle + (\sin 2\varphi_2 - \sin 2\varphi_3)\langle \sin 2\varphi\rangle] \ , \tag{3.31}$$

and the assumption of a symmetrical behaviour, i.e. $\cos 2\varphi_2 = \cos 2\varphi_3$ and $\cos 6\varphi_2 = \cos 6\varphi_3$, we obtain

$$\frac{\partial E_{\mathrm{tot}}}{\partial \xi_2} = -\frac{MVH^2}{4H_{\mathrm{ex}}}[\sin 2\alpha(\sin 2\varphi_3 - \sin 2\varphi_2)] + MVH_{\mathrm{dest}}(\sin 2\varphi_2 - \sin 2\varphi_3)\langle \sin 2\varphi\rangle \tag{3.32}$$

with a minimum for E_{tot} as for the three-domain case, see Eq. (3.17), at

$$\langle \sin 2\varphi \rangle = -\frac{H^2 \sin 2\alpha}{4H_{\mathrm{ex}}H_{\mathrm{dest}}} = -\frac{H^2}{H_{\mathrm{MD}}^2}\sin 2\alpha \ . \tag{3.33}$$

For $\frac{\partial E_{\mathrm{tot}}}{\partial \varphi_2}$ with the same assumptions, we obtain

$$\begin{aligned}\frac{\partial E_{\mathrm{tot}}}{\partial \varphi_2} =& MV\xi_2[-H_{\mathrm{a}}\sin 6\varphi_2 \\ &- \frac{H^2}{2H_{\mathrm{ex}}}\sin 2(\varphi_2-\alpha) \\ &+ 2H_{\mathrm{dest}}(\cos 2\varphi_2\langle\sin 2\varphi\rangle - \sin 2\varphi_2\langle\cos 2\varphi\rangle)] \ . \end{aligned} \tag{3.34}$$

We use Eq.(3.33) to replace the $\langle \sin 2\varphi\rangle$, set the derivative to zero, and end up with the result

$$\langle \cos 2\varphi \rangle = -\frac{H^2}{H_{\mathrm{MD}}^2}\cos 2\alpha - \frac{2H_{\mathrm{ex}}H_{\mathrm{a}}}{H_{\mathrm{MD}}^2}(4\cos^2 2\varphi_2 - 1) \ . \tag{3.35}$$

Since $H_{\mathrm{ex}}H_{\mathrm{a}}$ is much smaller than H_{MD}^2, we neglect the second term in Eq.(3.35) and obtain

$$\langle \cos 2\varphi \rangle = -\frac{H^2}{H_{\mathrm{MD}}^2} \cos 2\alpha \ , \tag{3.36}$$

which is the same result as in the three-domain case, see Eq. (3.16). With Eqs.(3.1) and (3.2), we calculate ρ_{long} and ρ_{trans} for the two-domain case, using $\xi_3 = 1 - \xi_2$ and $\langle \cos 2\varphi \rangle = \cos \varphi_2$, and obtain the same

$$\rho_{\mathrm{long}} = \rho_0 + \frac{\rho_1}{2} - \frac{\rho_1}{2} \frac{H^2}{H_{\mathrm{MD}}^2} \cos 2\alpha \ , \tag{3.37}$$

$$\rho_{\mathrm{trans}} = -\frac{\rho_3}{2} \frac{H^2}{H_{\mathrm{MD}}^2} \sin 2\alpha \ . \tag{3.38}$$

So we see, that the dependences for the three- and for the two-domain case are the same. The resistivity shows a 180°-periodic oscillation with an amplitude proportional to H^2. For external fields approaching the monodomain field, we have to take into account that in the two-domain case the remaining staggered vectors $\mathbf{l}_2$ and $\mathbf{l}_3$ undergo a rotation to result in the perpendicular alignment to the external field. Therefore, we must not put in fixed φ_2 and φ_3 as for the three-domain case but assume a symmetric rotation for $\mathbf{l}_2$ and $\mathbf{l}_3$.

3.2.3 Monodomain regime for $H \geq H_{\mathrm{MD}}$

For $H \geq H_{\mathrm{MD}}$, we end up with one domain that follows the field rotation, because in the equations for ρ_{long} and ρ_{trans} in both the three and the two-domain case, $\frac{H^2}{H_{\mathrm{MD}}^2}$ becomes unity

$$\rho_{\mathrm{long}} = \rho_0 + \frac{\rho_1}{2} - \frac{\rho_1}{2} \cos 2\alpha \ , \tag{3.39}$$

$$\rho_{\mathrm{trans}} = -\frac{\rho_3}{2} \sin 2\alpha \ . \tag{3.40}$$

Increasing the external field cannot increase the SMR amplitude any more.

3.3 Summary

We illustrate this scenario for two angles α (Fig. 3.2) and discuss the expected behaviour of the longitudinal resistivity ρ_{long}.

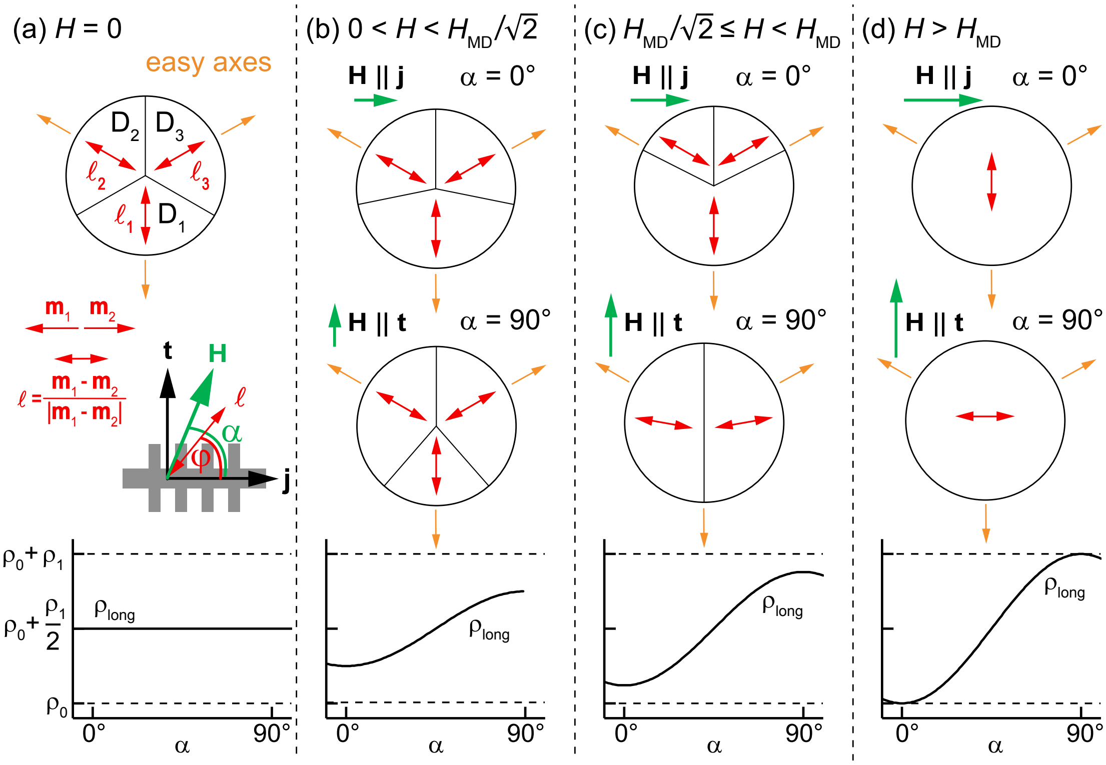

Figure 3.2: Vizualization of the theoretic model. Red arrows $\mathbf{l} = \mathbf{m}_1 - \mathbf{m}_2$ show the directions of the sublattice magnetizations for the three domains D_1 - D_3. With increasing external field $\mathbf{H}$ along the current direction $\mathbf{j}$ up to the critical field H_{MD}, only the domain walls are moving (top row, $\alpha = 0°$ where α defines the angle between $\mathbf{H}$ and $\mathbf{j}$). In the second row ($\alpha = 90°$), for $H = H_{\mathrm{MD}}/\sqrt{2}$ D_1 vanishes and up to H_{MD} the $\mathbf{l}_1$ and $\mathbf{l}_2$ rotate into the final monodomain state which is reached for the two domains for $H \geqslant H_{\mathrm{MD}}$. In the bottom row, the longitudinal SMR signal expected from this model for each regime of the external field H is shown. The amplitude increases up to the monodomain field where it reaches a constant maximum value.

In the absence of a magnetic field (Fig. 3.2 (a)), the sample consists of three AFM domains, equal in fraction. Their staggered vectors are aligned along the easy axes at angles of 120° with respect to each other. The resulting resistivity ρ_{long} of the Pt Hall bar is independent of α and is higher than ρ_0 for a single layer of Pt. Calculating ρ_{long} from Eq. (3.1) with $\xi_1 = \xi_2 = \xi_3 = 1/3$ and $\varphi_1 = 270°, \varphi_2 = 150°, \varphi_3 = 30°$ results in a value of $\rho_{\mathrm{long}} = \rho_0 + \rho_1/2$. Increasing the magnetic field up to $H = H_{\mathrm{MD}}/\sqrt{2}$ (Fig. 3.2 (b)) does not affect the domain orientation, but changes the domain fractions. For $\alpha = 0°$, D_1 is energetically favourable compared to D_2 and D_3, because $\mathbf{l}_1$ is perpendicular to $\mathbf{H}$ and therefore D_1 grows with increasing field. In contrast for $\alpha = 90°$, $\mathbf{l}_1$ is parallel to $\mathbf{H}$ and therefore D_2 and D_3 are the energetically favourable, increasing domains. This leads to a characteristic $-\cos 2\alpha$ dependence of ρ_{long}.

For higher external fields of $H_{\mathrm{MD}}/\sqrt{2} < H < H_{\mathrm{MD}}$ (Fig. 3.2 (c)), for $\alpha = 0°$, D_1 increases further until D_2 and D_3 vanish, resulting in a monodomain state. For $\alpha = 90°$ at $H = H_{\mathrm{MD}}/\sqrt{2}$, D_1 vanishes and $\mathbf{l}_{2,3}$ in the two remaining, energetically equal domains D_2 and D_3 start to rotate. The rotation also leads to a monodomain state at $H = H_{\mathrm{MD}}$ with $\mathbf{l}$ of the remaining domain perpendicular to $\mathbf{H}$.

For field magnitudes of $H > H_{\mathrm{MD}}$ (Fig. 3.2 (d)), the remaining domain rotates with the external field and the SMR amplitude reaches its maximum. The dependence of the SMR amplitude on the field is $(H/H_{\mathrm{MD}})^2$ for $H \leqslant H_{\mathrm{MD}}$. We note that only a change in domain fraction causes the $-\cos 2\alpha$ dependence of ρ_{long} at small magnetic fields, without rotation of the staggered vectors $\mathbf{l}_{\mathrm{k}}$.

This model was developed for the easy plane AFM NiO and will be published in [46].

Chapter 4

Spin Hall magnetoresistance in NiO|Pt bilayers

We present the SMR in NiO|Pt bilayers. We start with the material properties of the AFM NiO and the fabrication of the samples, before we show the results of the ADMR and field dependent measurements, that are performed to investigate the SMR effect. Finally, we conclude with an explanation of the experimental data applying the theoretical model for a three-domain AFM, presented above in chapter 3.

4.1 Material properties of NiO

NiO represents a prototypical antiferromagnetic insulator with a Néel temperature of 523 K [54] crystallizing in a simple, cubic sodium chloride structure (Fig. 4.1). The Ni^{2+} spins (red and blue in Fig. 4.1) align ferromagnetically along the cubic $\langle 11\overline{2} \rangle$ directions within the $\{111\}$ planes and antiferromagnetically between neighbouring $\{111\}$ planes [55–57]. The $\langle 11\overline{2} \rangle$ directions represent magnetically easy directions as illustrated in Fig. 4.2. In the absence of a magnetic field $\mathbf{H}$, NiO forms three antiferromagnetic domains (D_1 - D_3), containing spins in opposite directions from the neighbouring $\{111\}$ planes.

The transition from the paramagnetic to the antiferromagnetic phase at the Néel temperature is accompanied by a structural distortion from cubic to slightly rhombohedral [58]. However, this does not influence the fact, that the $\{111\}$ planes containing ferromagnetically ordered spins are parallel to each other and perpendicular to the diagonal of the rhombohedron. Therefore we neglect the rhombohedral distortion and consider the AFM NiO as cubic in the following. The bulk lattice

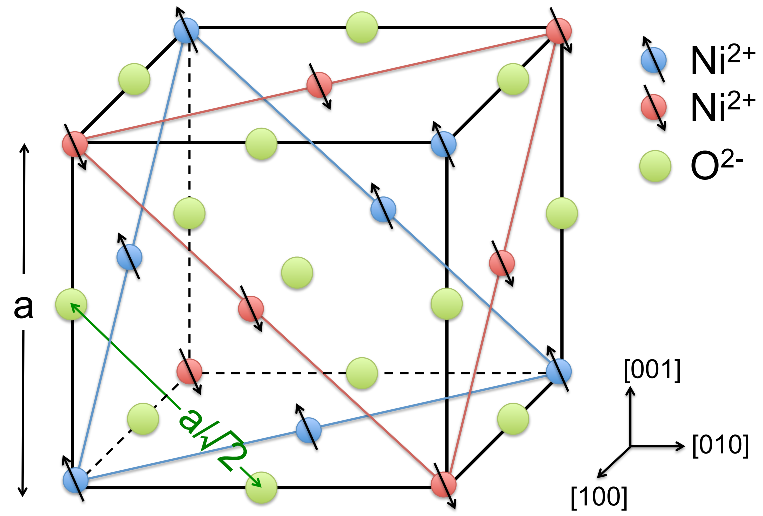

Figure 4.1: NiO crystal structure. The green oxygen ions are centered on the edges and in the cube and the nickel ions in the corners and the center of each face. The red and the blue triangle show the {111} planes with parallel oriented Ni spins.

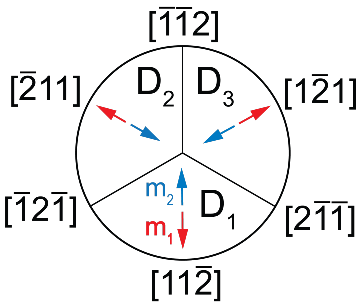

Figure 4.2: NiO domain structure with three domains D_1 - D_3 in the {111} planes. Each domain consists of two magnetic sublattices $\mathbf{m}_1$ (red) and $\mathbf{m}_2$ (blue), pointing in the indicated easy direchtions.

constant is a=0.417 nm and the distance between two oxygen ions (green in Fig. 4.1) in the {111} planes is $a/\sqrt{2}$ =0.295 nm.

The exchange and the anisotropy fields for NiO are reported to be $\mu_0 H_{\mathrm{ex}} = 968.4$ T and $\mu_0 H_{\mathrm{a}} = 11$ mT, respectively [57]. Furthermore, NiO is a material with a high magnetostriction value of 9×10^{-5} [59–62], which causes a significant destressing energy that has to be taken into account for the minimization of the free energy [50–53]. We will find later that the destressing field is $\mu_0 H_{\mathrm{dest}} = 46$ mT.

4.2 Fabrication of NiO|Pt thin films

We grow 120 nm thin NiO films via pulsed laser deposition (PLD) with a repetition rate of 2 Hz and a laser fluence of 2.5 J/cm^2 at 380 °C and 10 µbar oxygen pressure. Via electron beam evaporation (EVAP), a 2 nm thin Pt electrode is deposited in situ at room temperature and a base pressure of 6.7×10^{-7}mbar on top of the sample. Detailed information on PLD and EVAP can be found in the appendix.

We use (0001)-oriented Al_2O_3 substrates for the (111)-oriented growth of NiO. Al_2O_3 has a hexagonal crystal structure with lattice parameters of $a = 0.4763$ nm and $c = 1.3003$ nm. As in epitaxial growth the oxygen sublattice continues [63, 64], we can calculate a mismatch ε_{O} of the oxygen lattice, comparing the distances of two oxygen atoms in the (0001) plane of Al_2O_3 ($\delta_{\mathrm{O,Al_2O_3}} = 0.275$ nm [65]) and in the (111) plane of NiO ($\delta_{\mathrm{O,NiO}} = a_{\mathrm{NiO}}/\sqrt{2} = 0.295$ nm) of

$$\varepsilon_{\mathrm{O}} = \frac{\delta_{\mathrm{O,NiO}} - \delta_{\mathrm{O,Al_2O_3}}}{\delta_{\mathrm{O,Al_2O_3}}} = 7.3\,\% \ . \tag{4.1}$$

Therefore, we expect a relaxed growth of NiO on the sapphire substrate.

We employ X-ray diffraction to characterize the crystallographic structure of our samples. The out-of-plane $2\Theta-\omega$ scan shows only reflections which can be attributed either to the substrate or the film (Fig. 4.3). We find the expected (000l) reflections from the Al_2O_3 substrate and the (hkl) reflections (h=k=l) from the NiO thin film, evidencing that NiO[111]||Al_2O_3[0001]. In addition, a broad feature is observed which we attribute to the Pt top electrode. No secondary phases are detected. Via Bragg's law (Eq. A.1), using the three NiO reflections at $\Theta_{111} = 18.69°$, $\Theta_{222} = 39.85°$ and $\Theta_{333} = 73.97°$, we calculate the same value for the distance between the NiO {111} planes to $d_{\mathrm{NiO}} = 0.240$ nm. The coincidence in d for the three reflections shows that systematic errors are small. From the literature value for

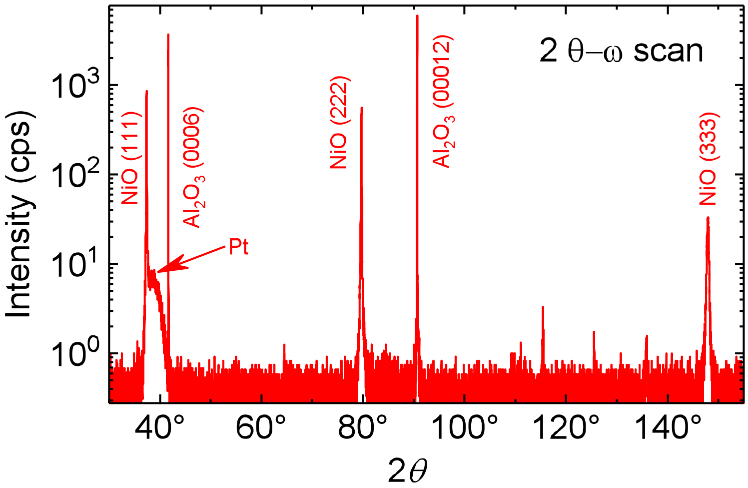

Figure 4.3: X-ray diffraction diagram. The $2\Theta - \omega$ scan shows (0006) and (00012) reflections of the Al_2O_3 substrate at $2\Theta = 41.65°$ and $90.67°$. The (111), (222) and (333) NiO film reflections are located at $2\Theta = 37.38°$, $2\Theta = 79.69°$ and $2\Theta = 147.94°$. The feature around $2\Theta = 40°$ results from the Pt electrode. The intensities are given in counts per second (cps).

the NiO lattice constant, we calculate the distance between two {111} planes to $d_{\mathrm{NiO,literature}} = d_{\mathrm{NiO}}/\sqrt{3} = 0.241\,\mathrm{nm}$. Since this coincides well with our measurement we conclude that the thin film grows out-of-plane relaxed as expected. Fig. 4.4 is a detailed view of the NiO (111)- and the Al_2O_3 (0006) reflection, as well as a broader feature. We assign this to the Pt top electrode, since cubic Pt with a bulk lattice constant of 0.3920 nm [66] shows a (111) reflection at 39.80°.

For the in-plane orientation, we expect NiO$[1\bar{1}0]||Al_2O_3[10\bar{1}0]$. To check this orientation and to calculate the in-plane lattice constant d_{ip} we recorded reciprocal spacemaps (RSM) of the substrate and the film reflection, see Fig. 4.5. The NiO (402) reflection occurs at $q_{\mathrm{H}} = 2.782$ and $q_{\mathrm{L}} = 10.812$, after alignment to the $Al_2O_3(30\bar{3}12)$ reflection. From the NiO (402) we move in the reciprocal space map "downwards" along the hexagonal $[000\bar{1}]$ (corresponding to the cubic $[\bar{1}\,\bar{1}\,\bar{1}]$) direction to $q_{000L} = 0$ to reach the hypothetic NiO $(2\bar{2}0)$ reflection (Fig. 4.6 (a)). First we calculate the distance between the NiO $\{2\bar{2}0\}$ planes via the equation for a hexagonal lattice structure

$$\frac{1}{d_{hkl}^2} = \left[\frac{4}{3}(h^2 + k^2 + hk) + l^2 \left(\frac{a}{c}\right)^2\right] \frac{1}{a^2} \,. \tag{4.2}$$

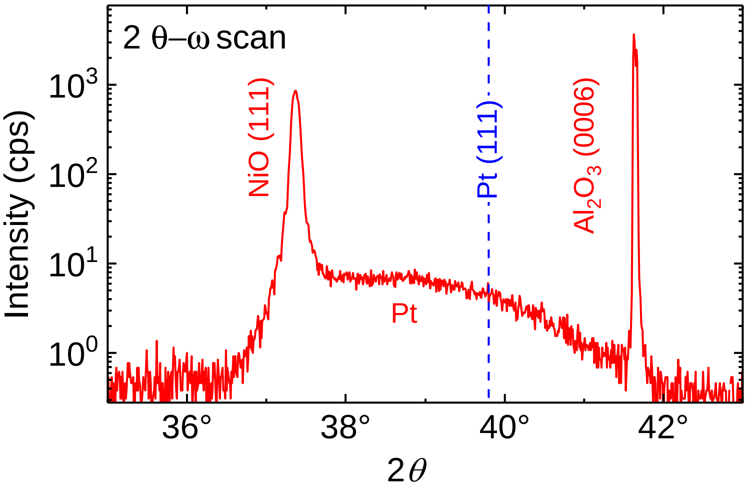

Figure 4.4: X-ray diffraction diagram on an enlarged scale. The $2\Theta - \omega$ scan shows the (0006) reflection of the Al_2O_3 substrate at $2\Theta = 41.65°$ and the (111) NiO film reflection at $2\Theta = 37.38°$. The (111) reflection for bulk Pt is expected at 39.80° (dashed blue line).

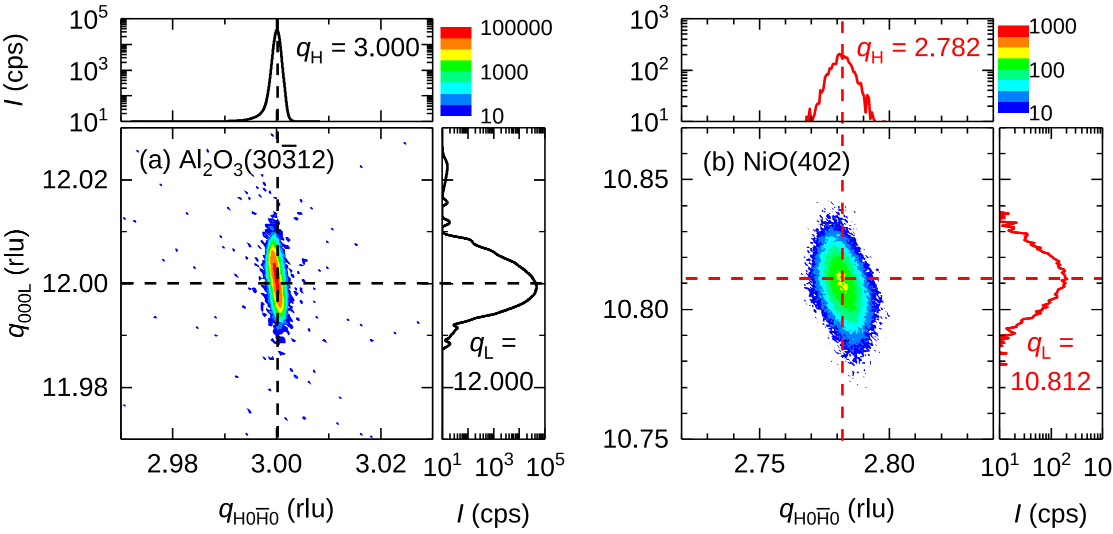

Figure 4.5: Reciprocal spacemaps and q-scans of (a) the Al_2O_3 $(30\bar{3}12)$ and (b) the NiO (402) reflection, found at $q_H = 2.782, q_L = 10.812$. The reciprocal scattering vectors q are given in reciprocal lattice units (rlu).

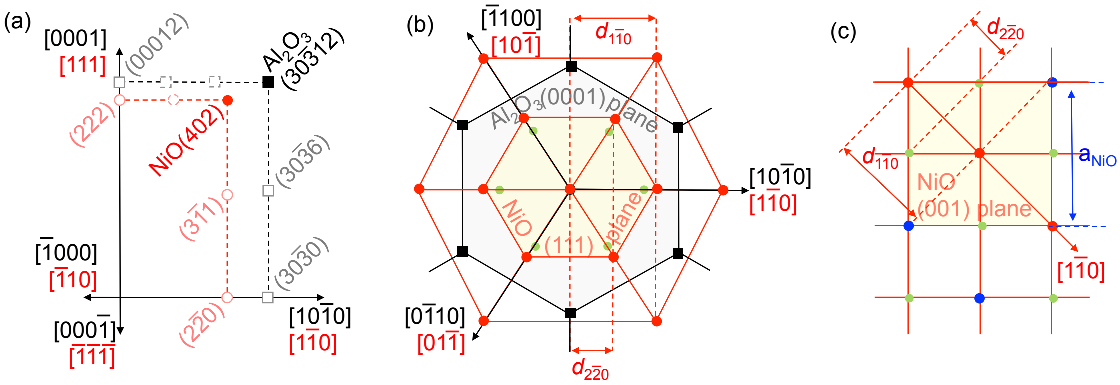

Figure 4.6: Epitaxial relations between NiO(111) and Al_2O_3(0001). (a) Expected reflections from Al_2O_3 (black) and NiO (red) in a schematic reciprocal space map (not to scale). (b) Top view on the Al_2O_3(0001) plane (grey shaded area) with the (0001)-oriented Al_2O_3 lattice (black) and the (111)-oriented NiO lattice (red). Oxygen ions are indicated in green. (c) Top view on the NiO(001) plane (yellow shaded area). The cubic lattice parameter a_{NiO} is indicated by a blue arrow.

We set the Miller indices $h,\ k,\ l$ to $h = 2.782, k = l = 0$ for the film, but take a and c for the hexagonal Al_2O_3, as we aligned on the hexagonal sapphire substrate. We obtain $d_{\{2\bar{2}0\}} = 0.1483\,\mathrm{nm}$ for the distance between the corresponding $\{2\bar{2}0\}$ planes. The distance between the $\{1\bar{1}0\}$ planes is $2 \times d_{\{2\bar{2}0\}} = 0.2966\,\mathrm{nm}$ (Fig. 4.6 (b)). For the in-plane lattice constant we are interested in the distance between the $\{100\}$ planes (Fig. 4.6(c)), so we need to multiply with $\sqrt{2}$ and obtain $d_{\mathrm{ip}} = 0.419\,\mathrm{nm}$. As well as for the oop lattice constant we find that the difference to the bulk lattice constant of $d_{\mathrm{ip,literature}} = 0.417\,\mathrm{nm}$ is very small and conclude that the thin film grows relaxed.

The rocking curve of the NiO (111) reflection (Fig. 4.7) shows a full width at half maximum (FWHM) of 0.029°. This indicates a high quality thin film with a low mosaic spread.

To determine the layer thickness, we apply X-ray reflectometry from $2\Theta = 0.5°$ to $2\Theta = 5°$ (Fig. 4.8). The small oscillations originate from the thicker NiO film, the larger oscillations from the thin Pt electrode. With a simulation of the experimental data using the software LEPTOS, we obtain the thicknesses $t_{\mathrm{NiO}} = 120\,\mathrm{nm}$ and $t_{\mathrm{Pt}} = 2\,\mathrm{nm}$ and a low surface roughness below 0.8 nm (rms value).

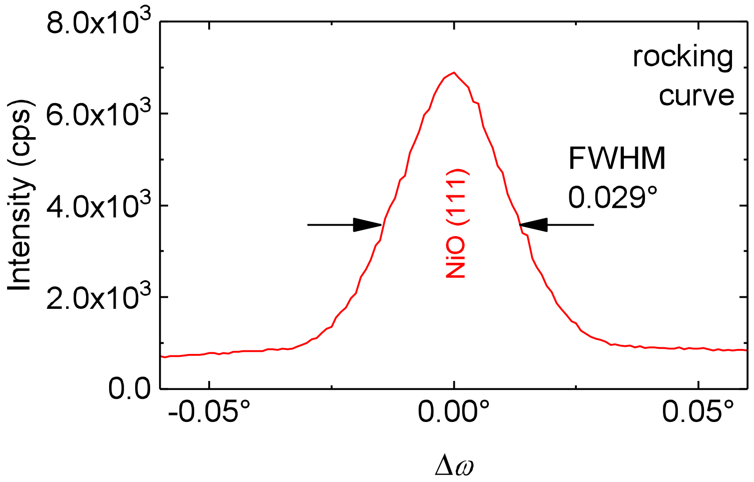

Figure 4.7: X-ray rocking curve around the NiO (111) reflection with a full width at half maximum (FWHM) of 0.029°.

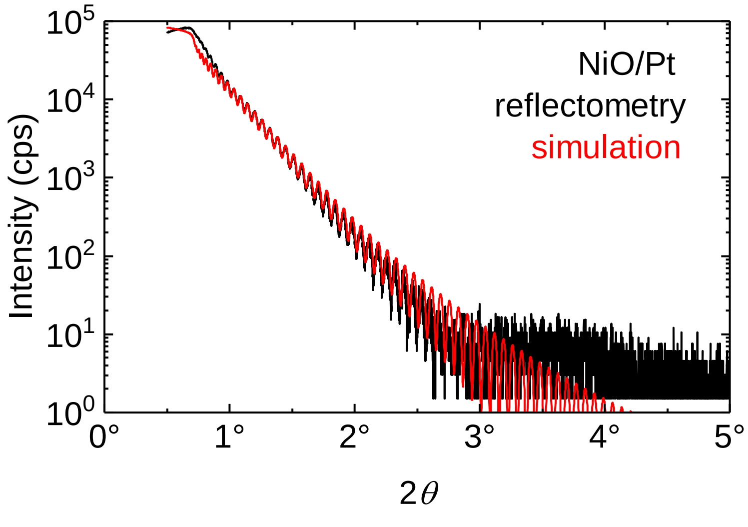

Figure 4.8: X-ray reflectometry to determine the thicknesses of the bilayer. The red curve was fitted to the black experimental curve using the software LEPTOS.

4.3 Magnetoresistance (MR) measurements

Via optical lithography and Ar ion milling, the sample is patterned into a Hall bar mesa structure with a width of $w = 80\,\mu$m and a contact separation of $l_{\mathrm{long}} = 600\,\mu$m for the longitudinal and $l_{\mathrm{trans}} = 80\,\mu$m for the transverse angle dependent (ADMR) measurements. For the Hall bar geometry (Fig. 2.4) the longitudinal and transverse resistivities ($\rho_{\mathrm{long}}, \rho_{\mathrm{trans}}$) are calculated from the longitudinal and the transverse voltages V_{long} and V_{trans} as

$$\rho = \frac{V\, w\, t_{\mathrm{Pt}}}{I\, l}\ . \tag{4.3}$$

V is measured with a standard four-probe technique using a dc current of $I = 100\,\mu$A and a current-reversal method [41]. After each measured voltage the current is inverted, taking six data points per voltage. By calculating the difference between the data points, taken at positive and negative current, we eliminate thermal voltages. The resistance of the Pt layer without an external field at room temperature is calculated to $\rho_{\mathrm{Pt}} = 2.30 \times 10^{-7}\,\Omega$m, in agreement to literature values for the resistivity of $2.40 \times 10^{-7}\,\Omega$m [34]. From resisitivity measurements, we aim to obtain an SMR signal in the range of $\leqslant 10^{-4}$. The Pt resistivity, however, sensitively depends on the temperature T (0.4 % per K at room temperature [67]) and causes a signal of the same order of magnitude if $\Delta T \geqslant 0.025$ K. This makes the following data collection quite challenging and requires to perform the experiments very carefully.

4.3.1 Angle and field dependent MR for in-plane rotations of the external magnetic field *H*

We perform angle dependent magnetoresistance (ADMR) measurements at 300 K by rotating an applied magnetic field $\mathbf{H}$ of constant magnitude in the (111)-plane of the NiO film. To eliminate any non-SMR related contributions to the resistivity, we plot the ADMR data normalized to the ρ_{long} value at $\alpha = 0^\circ$ ($\mathbf{j} \parallel \mathbf{h}$), which corresponds to the case, where $\mathbf{M}_{1,2} \parallel \mathbf{s}$ at high fields and the spin current is reflected, because no STT is possible (Fig. 2.3). Furthermore, we shift the normalized data $\rho_{\mathrm{long}}/\rho(0^\circ)$ by -1 to move the minimal $\rho_{\mathrm{long}}(0^\circ)$ to zero (Fig. 4.9). We find a characteristic 180° periodic oscillation, similar to the SMR in AFM, but shifted by 90°. The oscillation amplitude increases with increasing external magnetic field. This corresponds to our

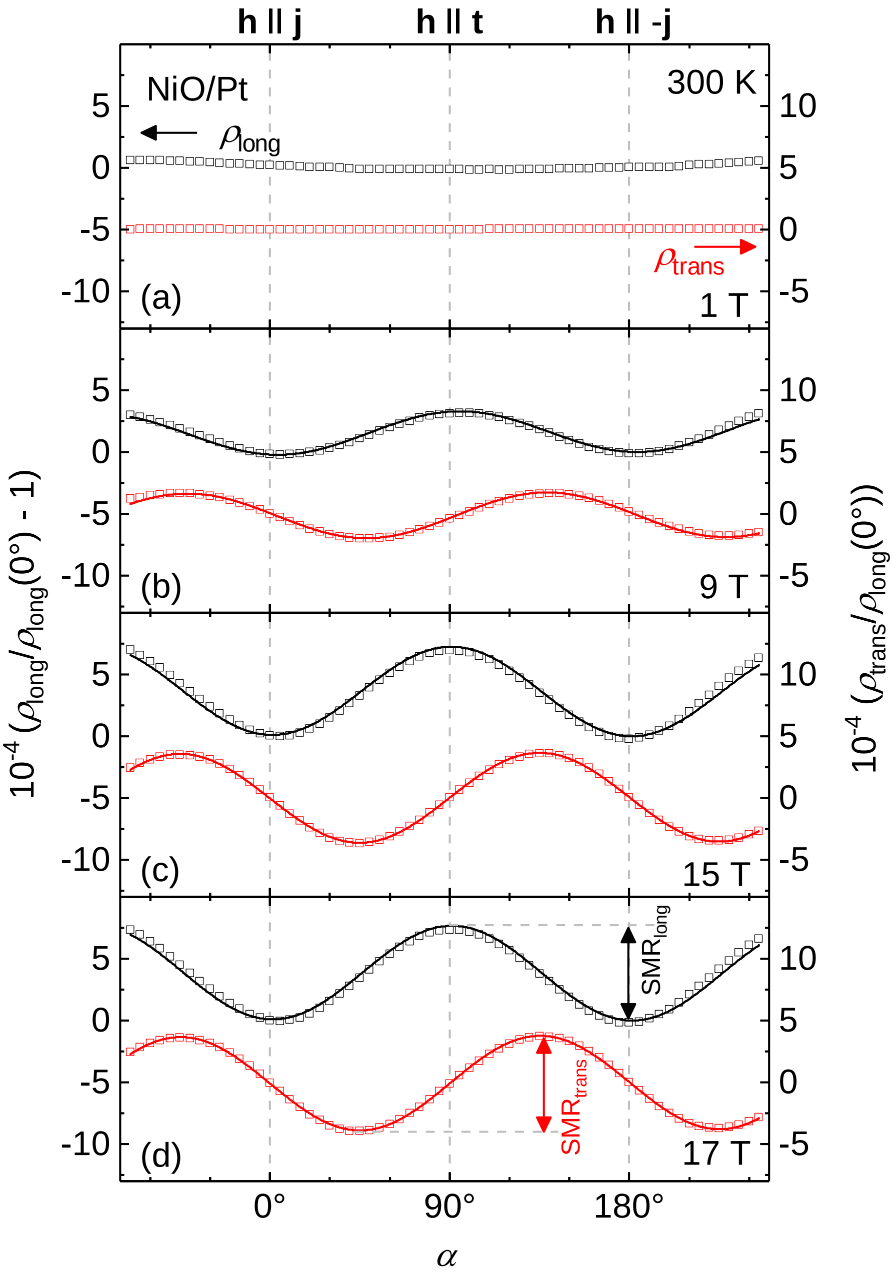

Figure 4.9: ADMR measurements of a NiO(111)/Pt bilayer, measured at 300 K at in-plane external magnetic field magnitudes of (a) 1 T, (b) 9 T, (c) 15 T, (d) 17 T. The normalized longitudinal resistivity ρ_{long} (black symbols, left axis) and transverse resistivity ρ_{trans} (red symbols, right axis) are plotted as a function of the magnetic field orientation α. The lines are fits to the data according to Eqs. (4.4) and (4.5).

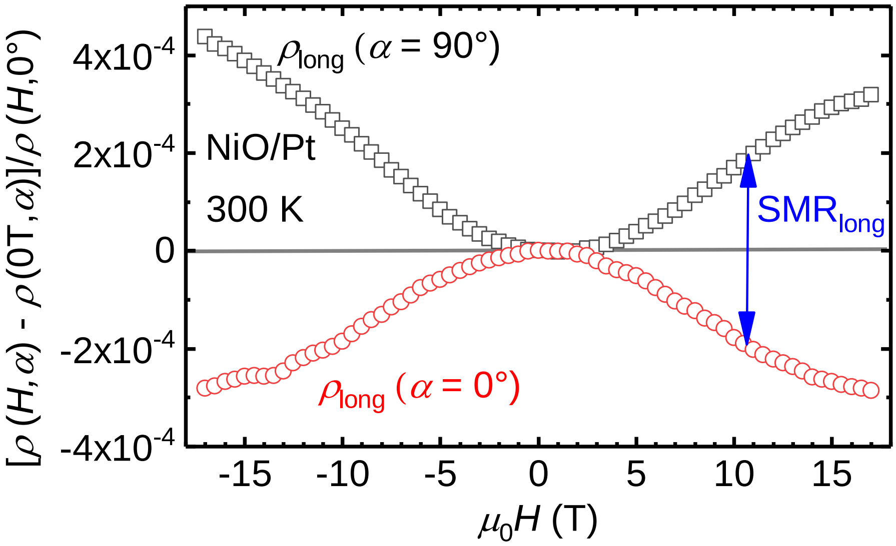

Figure 4.10: Field-dependent longitudinal resistivity $\rho_{\mathrm{long}}(H)$ of the NiO(111)/Pt bilayer normalized to $\rho_{\mathrm{long}}(H, 0°)$ after subtracting $\rho_{\mathrm{long}}(0\,\mathrm{T}, \alpha)$. The data were measured at 300 K for $\alpha = 90°$ ($\mathbf{H} \parallel \mathbf{t}$, black symbols) and $\alpha = 0°$ ($\mathbf{H} \parallel \mathbf{j}$, red symbols). The distance between the two curves corresponds to the longitudinal SMR amplitude (blue arrow).

expectations in the theoretical model, presented in chapter 3. The data are fitted, using

$$\frac{\rho_{\mathrm{long}}}{\rho_{\mathrm{long}}(0°)} - 1 = \frac{1}{2}\mathrm{SMR}_{\mathrm{long}}(H) - \frac{1}{2}\mathrm{SMR}_{\mathrm{long}}(H)\cos 2\alpha\ , \tag{4.4}$$

$$\frac{\rho_{\mathrm{trans}}}{\rho_{\mathrm{long}}(0°)} = -\frac{1}{2}\mathrm{SMR}_{\mathrm{trans}}(H)\sin 2\alpha\ . \tag{4.5}$$

$\mathrm{SMR}_{\mathrm{long}}(H)$ and $\mathrm{SMR}_{\mathrm{trans}}(H)$ are the longitudinal and the transverse SMR amplitudes. Increasing the constant magnetic field magnitude H from 9 T to 17 T (Fig. 4.9, (b-d)) shows that the SMR amplitudes are field dependent. The $\rho_{\mathrm{long}} \propto -\cos 2\alpha$, $\rho_{\mathrm{trans}} \propto -\sin 2\alpha$ dependence of the ADMR resisitivity shows the same behaviour as derived in chapter 3, indicating the validity of our three-domain model for the SMR in AFMs.

To further confirm this scenario, we measure the field dependence and perform magnetic field sweeps at fixed orientations ($\alpha = 0°$ and $\alpha = 90°$) of the magnetic field with respect to the crystallographic axes of NiO (i.e. at the minima and the maxima of the ADMR measurements) at 300 K (Fig. 4.10). The longitudinal resis-

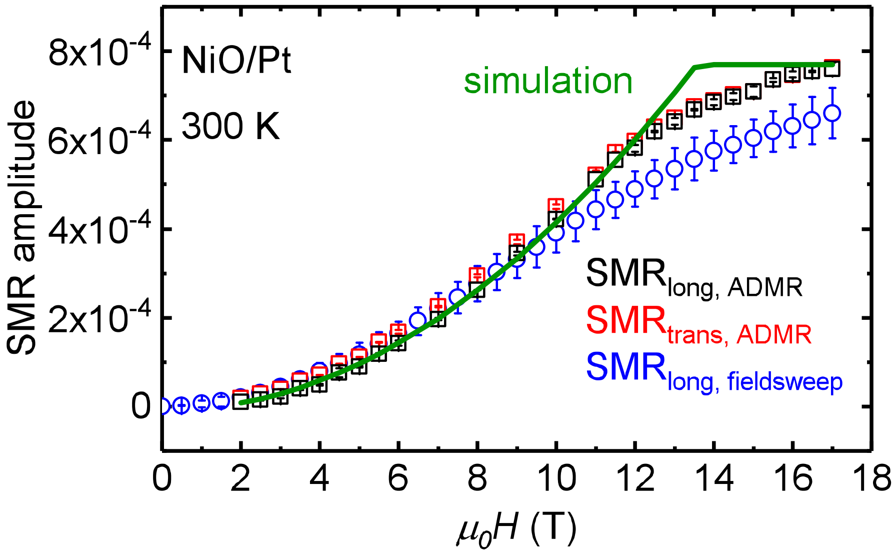

Figure 4.11: SMR amplitude of the NiO(111)/Pt bilayer obtained from ADMR measurements at 300 K at different external magnetic field magnitudes (cf. Fig. 4.9) using the longitudinal (black symbols) and transverse (red symbols) resistivities as well as data extracted from the fieldsweep measurements shown in Fig. 4.10 (blue symbols) as a function of the external magnetic field magnitude. The data are compared to a simulation, based on the theory, presented in chapter 3 (green line).

tivity is plotted after subtracting a constant value of $\rho_{\text{long}}(0\,\text{T}, \alpha)$ from both curves and dividing by the original $\rho_{\text{long}}(H, 0°)$. Because of the longer duration of the measurement, compared to the ADMR measurement, the sensitivity to temperature instabilities is increased for the fieldsweep and causes the slight asymmetry. With increasing field magnitude, the resistivity increases for $\alpha = 90°$ (black symbols) and decreases for $\alpha = 0°$ (red symbols). This corresponds well with our theory model and confirms our assumption of the AFM domain evolution (cf. Fig. 3.2).

In Fig. 4.11, we compare the SMR amplitudes $\text{SMR}_{\text{long}}(H)$ and $\text{SMR}_{\text{trans}}(H)$ (black and red symbols), derived from the fits of the ADMR measurements with the SMR amplitude from the fieldsweep (blue symbols). The error bars for the ADMR measurements are determined from the fitting algorithm and the average over different measurements per magnetic field value. For the fieldsweep, the error is dominated by the temperature instabilities as described above. For $H > 10\,\text{T}$, we find a deviation beween the results from the fieldsweep and the ADMR measurements larger than the error range, which we arrtibute to a slight deviation between the angle α in the fieldsweep and the real geometrical directions of the Hall bar. Following the model for the SMR in a three-domain AFM (Chapter 3), Olena Gomonay calculated simulation curves for the field dependence of the SMR amplitude from

$$\rho_{\text{long}} = \rho_0 + \frac{\rho_1}{2} - \frac{\rho_1}{2}\frac{H^2}{H_{\text{MD}}^2}\cos 2\alpha \ , \tag{4.6}$$

$$\rho_{\text{trans}} = -\frac{\rho_3}{2}\frac{H^2}{H_{\text{MD}}^2}\sin 2\alpha \ . \tag{4.7}$$

using different monodomain fields H_{MD}. The best fit was obtained for $H_{\text{MD}} = 13.4\,\text{T}$ (green curve in Fig. 4.11). Up to 12.5 T, we see a perfect agreement of the simulated H^2-dependence of the SMR amplitudes to the experimental data. The abrupt saturation of the SMR amplitude at $H > H_{\text{MD}}$ is not reflected in our data, mainly due to unavoidable imperfections of our NiO thin film, smearing out the transition to a monodomain state over a broad field range.

4.3.2 Angle dependent MR for out-of-plane rotations of the external magnetic field *H*

To complete the picture of the SMR effect in a three-domain AFM, we perform out-of-plane ADMR measurements of ρ_{long} - rotating a magnetic field of a constant magnitude of 7 T around the $\mathbf{j}$ (out-of-plane $\mathbf{j}$, oopj) - and around the $\mathbf{t}$ axis (oopt), see Fig. 4.12. As in the oopt rotation (red) we normalize the data to $\mathbf{h} \parallel \mathbf{j}$ at 0°, the resistance should be at the same level as for the ip rotation (black), corresponding to minimum STT for $\mathbf{M}_{1,2} \parallel \mathbf{s}$. Because of thermal drifts between the two measurments, however, we find a gap in the raw data that was subtracted. We also adjust the oopj (blue) to the oopt measurement such that they become equal at 90° for both $\mathbf{h} \parallel -\mathbf{n}$. There the external field points out of the easy planes in NiO and we assume that the anisotropy energy is dominant, resulting in the same multidomain state as for $H = 0\,\text{T}$ (see chapter 3). Then, the value from the ip rotation (black) at 90° ($\mathbf{h} \parallel \mathbf{t}$) corresponds very well to the one from the oopj measurement (blue) at 180°, where maximal STT is possible as $\mathbf{M}_{1,2} \perp \mathbf{s}$.

The SMR amplitude is calculated as the difference between the oopj and the oopt measurement at 0° and we find a good agreement to the SMR amplitude of the ip rotation which nicely justifies our data normalization procedures.

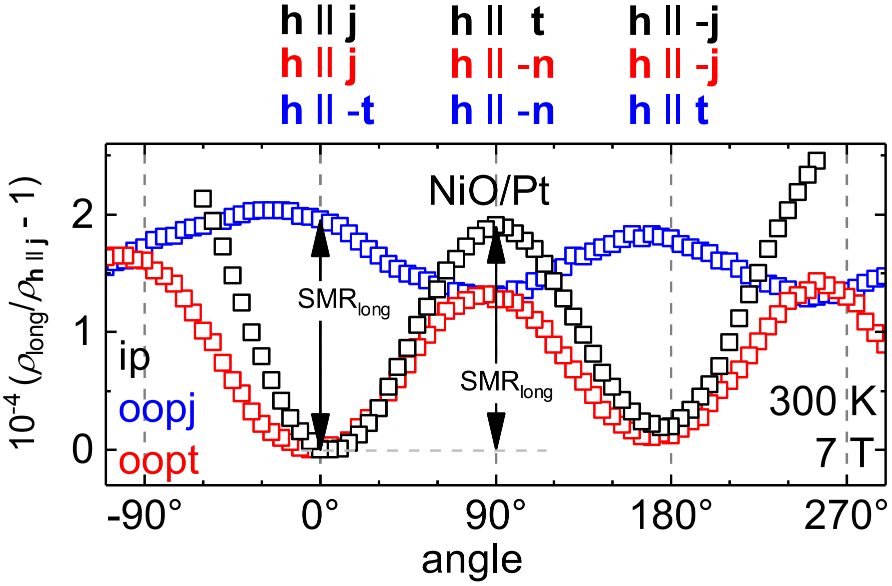

Figure 4.12: ADMR measurements of a NiO(111)/Pt bilayer, measured at 300 K at out-of-plane (oop) external magnetic field rotations at 7 T. The longitudinal resistivities ρ_{long} for rotations around the **j** axis (oopj, blue) and around the **t** axis (oopt, red) are both normalized to the value $\rho_{\mathrm{long}}(\mathbf{h}\|\mathbf{j})$ which corresponds to $\alpha = 0°$ in the ip rotation, that is shown as a comparison (black).

Chapter 5

Spin Hall magnetoresistance in α-Fe_2O_3 |Pt bilayers

Applying the same experimental procedures as for the NiO|Pt heterostructures, we investigate the SMR effect in Fe_2O_3|Pt bilayers. In this chapter, we present the material properties of the AFM α-Fe_2O_3, the fabrication of our thin films on sapphire substrates, and the results we obtained for the angle-dependent magnetoresistance measurements, that we study at temperatures from 15 K to 300 K.

5.1 Material properties

The electrical insulator α-Fe_2O_3 has a hexagonal crystal structure with the lattice parameters $a = 0.504\,\mathrm{nm}$ and $c = 1.375\,\mathrm{nm}$ [68]. It is an antiferromagnetic material with a Néel temperature of $T_\mathrm{N} = 950\,\mathrm{K}$, which becomes paramagnetic above T_N [69]. Another critical temperature is the Morin temperature T_Morin. For $T < T_\mathrm{Morin}$ the antiferromagnetic sublattices $\mathbf{M}_1$ and $\mathbf{M}_2$ are parallel and antiparallel to the c-axis, and for $T > T_\mathrm{Morin}$ they are lying in the (0001)-plane and are slightly canted [70]. The existance of the Morin transition in Fe_2O_3 (0001) oriented thin films represents a controversially discussed subject in research and is not always confirmed [69–73]. This makes it diffucult to obtain reliable vaues for the the exchange and the in-plane (0001) anisotropy fields. We assume $\mu_0 H_\mathrm{ex} = 1000\,\mathrm{T}$ and $\mu_0 H_\mathrm{a} = 10$ mT, respectively. T_Morin depends on the thickness of the Fe_2O_3 film. For 100 nm (250 nm, 500 nm) thick Fe_2O_3 the Morin transition was found at $T_\mathrm{Morin} \approx 180\,\mathrm{K}$ (225 K, 250 K) [69] and for bulk material at 263 K [74]. In contrast to NiO, the magnetostriction in Fe_2O_3 does not exceed 1×10^{-7} [75] and is, therefore, almost 3 orders of magnitude smaller than in NiO. As a result, Fe_2O_3 shows a much weaker destressing effect (cf. Chapter 3) and gets monodomain under the influence of much lower magnitudes of external magnetic fields, when they are applied in the magnetic easy (0001) plane. The monodomain state, however, is not reached up to 0.6 T [76], meaning that the destressing field is at least 0.06 mT.

5.2 Fabrication of $Fe_2O_3|Pt$ thin films

We grow 90 nm thin Fe_2O_3 films via pulsed laser deposition with a laser repetition rate of 2 Hz and a laser fluence of 2.5 J/cm^2 at 320 °C and 25 µbar oxygen pressure. Via electron beam evaporation, a 3.5 nm thin Pt electrode is deposited in situ at room temperature and a base pressure of 6.7×10^{-7}mbar on top of the sample.

For the epitaxial growth of Fe_2O_3, we use single crystalline substrates of Al_2O_3 (cf. section 4.2). Al_2O_3 has a hexagonal crystal structure with lattice parameters of $a = 0.4763\,\text{nm}$ and $c = 1.3003\,\text{nm}$. This results in a lattice mismatch of

$$\varepsilon_a = \frac{a_{\text{film}} - a_{\text{substrate}}}{a_{\text{substrate}}} = 5.8\,\% \quad \text{and} \quad \varepsilon_c = \frac{c_{\text{film}} - c_{\text{substrate}}}{c_{\text{substrate}}} = 5.7\,\% \; .$$

Because of this quite high mismatch we expect a relaxed growth. We are again interested in $Fe_2O_3|Pt$ bilayer samples with the Hall bar in the easy (0001) plane of the AFM, at least for $T_{\text{Morin}} < T < T_{\text{N}}$. To obtain (0001) oriented Fe_2O_3 we use Al_2O_3 (0001) substrates.

We employ X-ray diffraction to characterize the crystallographic structure of our samples. As in the NiO|Pt samples before, the $2\Theta - \omega$ scan shows only reflections which can be attributed either to the substrate or the film (Fig. 5.1). No secondary phases are detected. The Al_2O_3 (0006) and (00012) reflections are located at $\Theta = 20.84°$ and $\Theta = 45.36°$, the (0006) and (00012) film reflections at $\Theta = 19.69°$ and $\Theta = 42.36°$. So we calculate in the same way as for NiO the out-of-plane lattice parameter of $d_{\text{oop}}^{Fe_2O_3} = 1.372\,\text{nm}$ and obtain a very good agreement to the bulk lattice constant of $c_{Fe_2O_3} = 1.375\,\text{nm}$.

In Fig. 5.2, we show a detailed view of the $2\theta - \omega$ scan. The high crystalline quality of our Fe_2O_3 films is evidenced by observing satellites due to Laue oscillations around the Fe_2O_3 (0006) film reflection and the full width at half maximum (FWHM) of 0.027° of the rocking curve (Fig.5.3) which furthermore indicates a low mosaic spread.

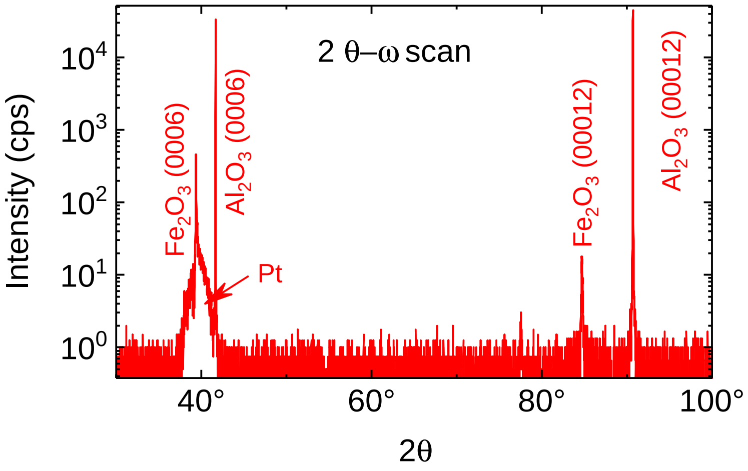

Figure 5.1: X-ray diffraction diagram. The $2\Theta - \omega$ scan shows (0006) and (00012) reflections of the Al_2O_3 substrate at $2\Theta = 41.68°$ and $90.72°$. The (0006) and (00012) film reflections are located at $2\Theta = 39.38°$ and $84.72°$. The feature around $2\Theta = 40°$ results from the Pt electrode. The intensities are given in counts per second (cps).

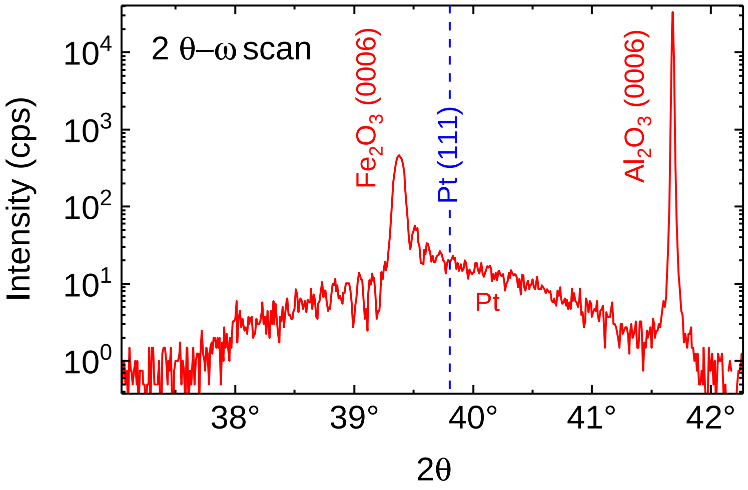

Figure 5.2: X-ray diffraction diagram on an enlarged scale. The $2\Theta - \omega$ scan shows the (0006) reflection of the Fe_2O_3 film and the Al_2O_3 substrate at $2\Theta = 39.38°$ and $41.68°$, respectively. The (111) reflection for bulk Pt is expected at 39.80° (dashed blue line).

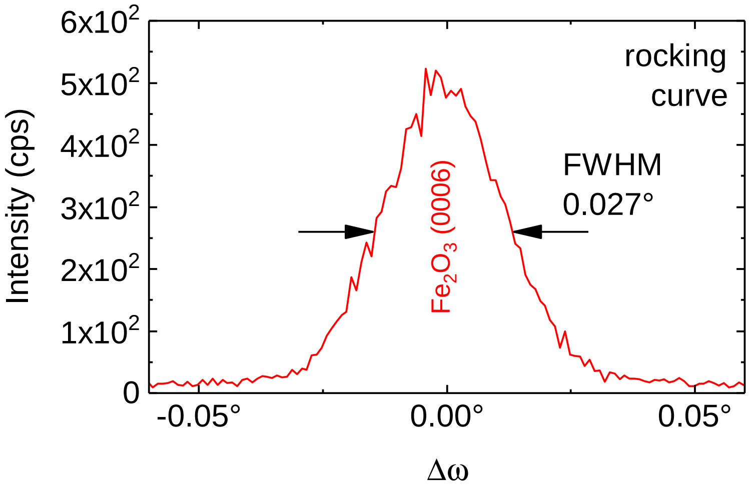

Figure 5.3: X-ray rocking curve around the Fe_2O_3 (0006) reflection with a full width at half maximum (FWHM) of 0.027°.

To calculate the in-plane lattice constant $d_{\mathrm{ip}}^{\mathrm{Fe_2O_3}}$, we record reciprocal spacemaps (RSM) of two substrate and film reflections, see Fig. 5.4. The Fe_2O_3 $(10\bar{1}10)$ reflection was found at $q_{\mathrm{H}} = 0.942, q_{\mathrm{L}} = 9.467$, when we align on the Al_2O_3 $(10\bar{1}10)$ reflection at $q_{\mathrm{H}} = 1$ and $q_{\mathrm{L}} = 10$. We calculate the distance between the $\{00010\}$ planes and compare the value with the oop lattice constant from the $2\theta - \omega$ scan. Using the equation for a hexagonal lattice structure (Eq. 4.2) with the Miller indices $\mathrm{l} = 9.467, \mathrm{h} = \mathrm{k} = 0$ for the film and the lattice parameters a,c for Al_2O_3, we obtain $d_{\{00010\}} = 0.1373\,\mathrm{nm}$. Multiplying by 10 gives the out-of-plane lattice constant $d_{\mathrm{oop}}^{\mathrm{Fe_2O_3}} = 1.373\,\mathrm{nm}$, which is in good agreement to the literature value $c_{\mathrm{Fe_2O_3}} = 1.375\,\mathrm{nm}$.

For the in-plane lattice constant, we are interested in the distance between the $\{10\bar{1}0\}$ planes, so we use $\mathrm{h} = 0.942, \mathrm{l} = \mathrm{k} = 0$ and obtain $d_{\{10\bar{1}0\}} = 0.437\,\mathrm{nm}$. This value has to be multiplied by $1/\cos 30° = 2/\sqrt{3}$ (Fig. 5.5) to calculate $d_{\mathrm{ip}}^{\mathrm{Fe_2O_3}} = 0.505\,\mathrm{nm}$, which is in almost perfect agreement to the bulk ip lattice constant $a_{\mathrm{Fe_2O_3}} = 0.504\,\mathrm{nm}$. So we can conclude that our Fe_2O_3 grows fully relaxed in-plane.

Analoguous to the characterization of the NiO|Pt bilayer, we determine the layer thicknesses via X-ray reflectometry (Fig. 5.6). With a simulation of the experimental data using the software LEPTOS, we obtain the thicknesses $t_{\mathrm{Fe_2O_3}} = 90\,\mathrm{nm}$ and $t_{\mathrm{Pt}} = 3.0\,\mathrm{nm}$ with a roughness below 1.1 nm (rms value) of the Fe_2O_3 thin film.

With superconducting quantum interference device (SQUID) magnetometry, we determine the temperature dependence of the magnetization M of the sample (not

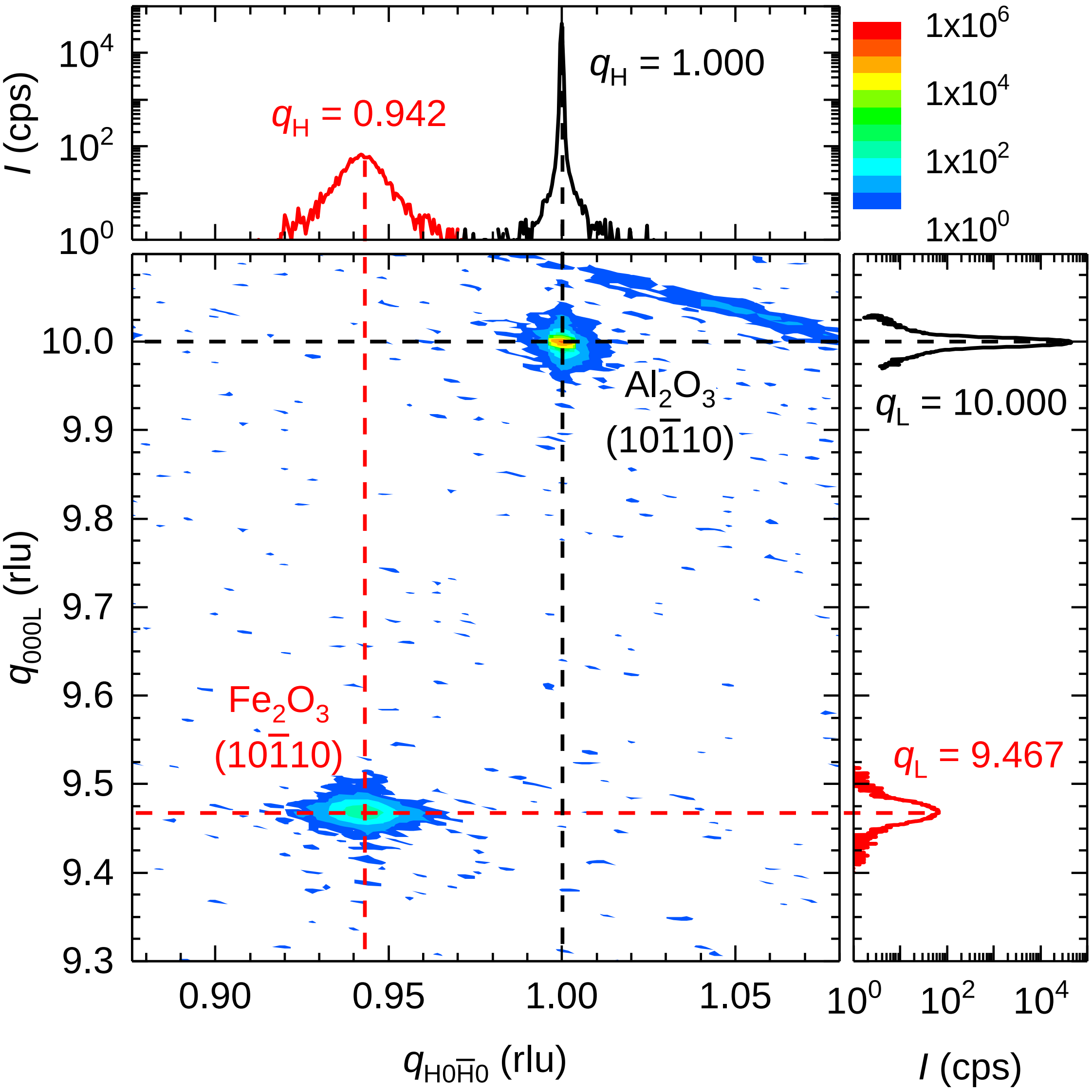

Figure 5.4: Reciprocal spacemaps and q-scans of the Al_2O_3 $(10\bar{1}10)$ and the Fe_2O_3 $(10\bar{1}10)$ reflection, found at $q_H = 0.942, q_L = 9.467$.

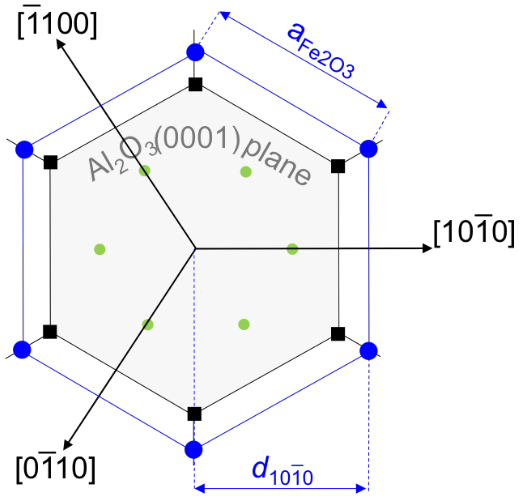

Figure 5.5: Epitaxial relation between Fe_2O_3(0001) and Al_2O_3(0001). Top view on the Al_2O_3(0001) plane (grey shaded area) with the (0001)-oriented Al_2O_3 lattice (black) and the (0001)-oriented Fe_2O_3 lattice (blue). Oxygen ions are indicated in green.

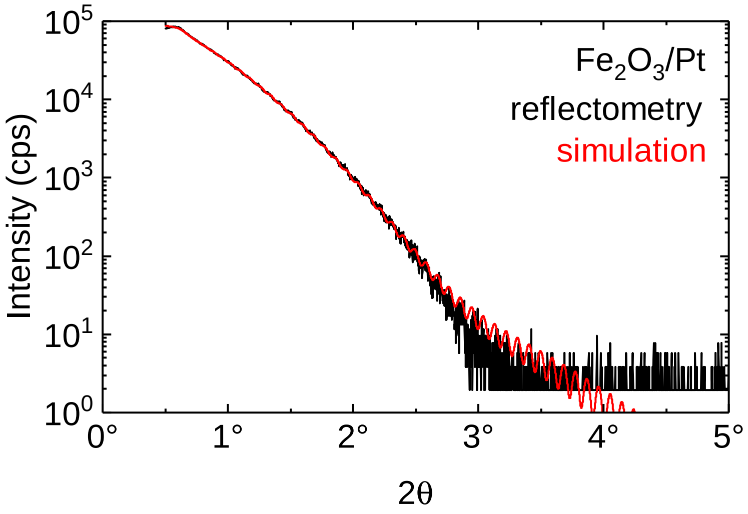

Figure 5.6: X-ray reflectometry to determine the thicknesses of the bilayer. The black experimental curve was fitted with the red curve using the software LEPTOS.

shown here). In contrast to the predicted Morin transition, we do not observe a reorientation of the antiferromagnetic sublattice down to 3 K. This is in agreement with other reports [70], where no Morin transition was found in Fe_2O_3 (0001) oriented, 100 nm thin films.

5.3 Magnetoresistance (MR) measurements

Via optical lithography and Ar ion milling, we fabricate Hall bars in the same way as for the MR measurements in NiO. We measure again with the standard four probe technique, described in chapter 4, and Eq. (4.3) is used to calculate the resistances from the measured voltages at a dc current of $I = 100\,\mu\mathrm{A}$ and for the same Hall bar geometry as in chapter 4.

We perform angle dependent magnetoresistance (ADMR) measurements at 15 K, 100 K, 150 K and 300 K by rotating an applied magnetic field of constant magnitude in the (0001)-plane of the Fe_2O_3 film. The measurements were carried out while rotating the sample in the variable temperature insert of a superconducting magnet cryostat (for details see Appendix). The data were fitted according to Eqs. (4.4) and (4.5).

5.3.1 Angle dependent MR for in-plane rotations of the external magnetic field H at 300 K

Since the magnetostriction for Fe_2O_3 is almost three orders of magnitude smaller ($\leqslant 1 \times 10^{-7}$ [75]) than for NiO (9×10^{-5} [52]), the monodomain field is smaller. So we started to measure at very low field magnitudes at 300 K, see Fig. 5.7. For 0.01 T and 0.1 T, we detect no reproducible angle-dependent signal (Fig. 5.7 (a,b)). For higher field magnitudes, we see the same characteristic oscillation as for NiO|Pt. Compared to the FMI the maxima and minima of the 180°-periodic oscillation are again shifted by 90° and can be explained by the theoretical model presented in chapter 3. The remarkable difference to NiO|Pt is, that the oscillation amplitude for 0.3 T (Fig. 5.7 (c)) is with 2×10^{-3} already at a much higher value than in the monodomain case for NiO|Pt (chapter 4). Besides from 1 T (Fig. 5.7 (d) and Fig. 5.8 (a)) to 3 T the SMR amplitude stagnates. This observation indicates that the monodomain situation, depicted earlier in Fig. 4.9(d), is for Fe_2O_3 indeed reached already at 1T and that the staggered magnetization rotates simultaneously with the

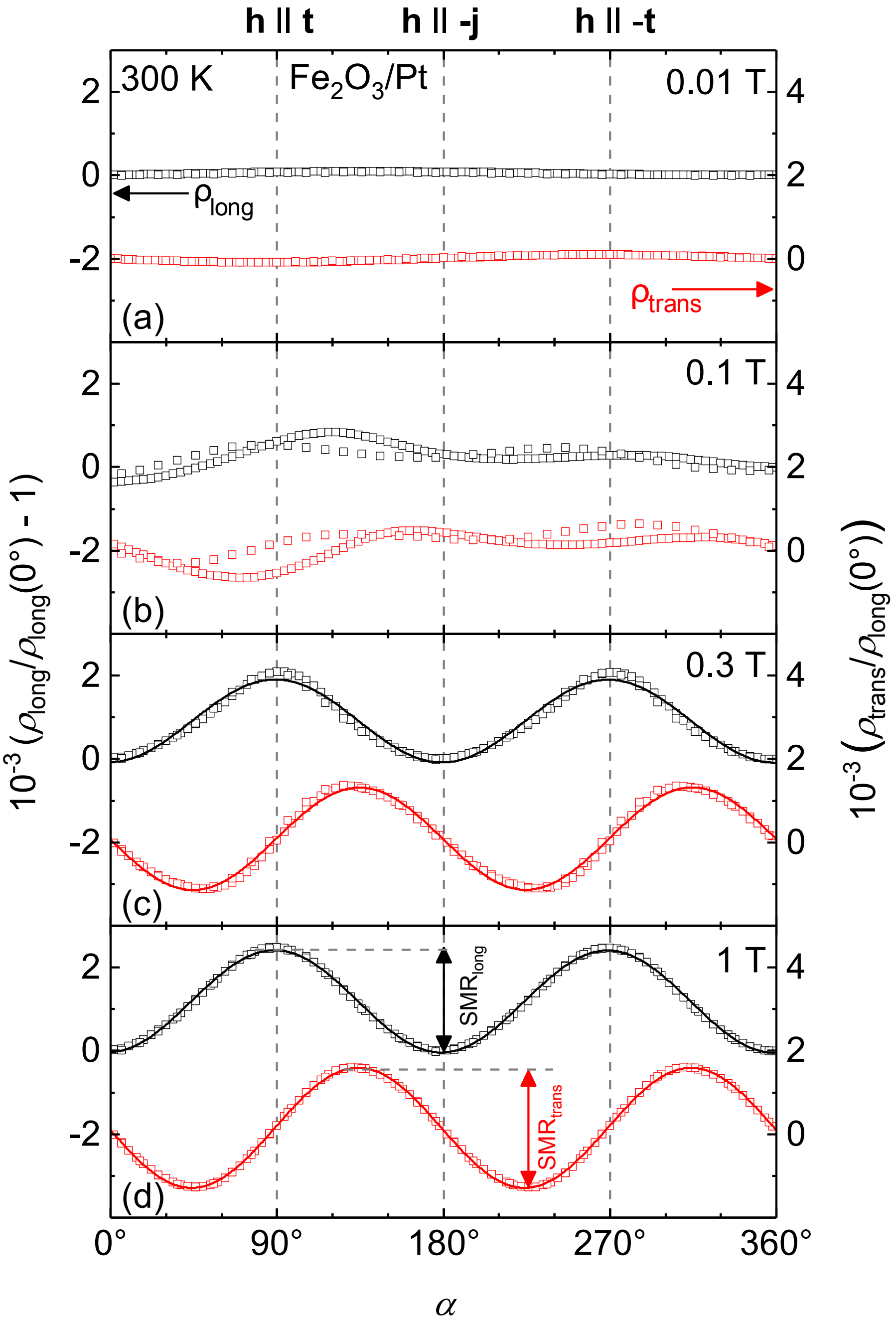

Figure 5.7: ADMR measurements of a $Fe_2O_3(0001)/Pt$ bilayer, measured at 300 K at in-plane external magnetic field magnitudes of (a) 0.01 T, (b) 0.1 T, (c) 0.3 T, (d) 1 T. The normalized longitudinal resistivity ρ_{long} (black symbols, left axis) and transverse resistivity ρ_{trans} (red symbols, right axis) are plotted as a function of the magnetic field orientation α. The data were collected while sweeping α first upwards to 360° at an increment of 3° and then downwards back to 0° at an increment of 10°. The lines are fits to the data according to Eqs. (4.4) and (4.5).

external magnetic field. Higher field magnitudes up to 17 T (Fig. 5.8 (b-d)) even evoke a slight decrease of SMR amplitude. We assign this decrease to an increased canting of the AFM sublattices [70] that contributes to the SMR in the same way as a ferromagnetic sublattice, as the net canted moment is parallel to H.

5.3.2 Temperature dependence of the ADMR measurements

Because of the reported Morin transition at around 180 K in thin films [69], we studied the SMR effect in Fe_2O_3 also at low temperatures. If a Morin transition with a reorientation of the Fe_2O_3 sublattice magnetizations along [0001] (i.e. out-of-plane) was present we would expect a vanishingly small SMR signal. Fig. 5.9 shows ADMR measurements, rotating a constant magnetic field of 1 T, 5 T, 9 T and 13 T, at 15 K, i.e. well below T_{Morin}, in the Fe_2O_3 (0001) plane (ip). Surprisingly, the results for 15 K and 300 K are almost the same. In Fig. 5.10, an overview of the SMR amplitudes versus field for all ip measurements at 300 K and 15 K is shown. We conlude, that our ADMR measurements, in agreement to the results from SQUID magnetometry, do not indicate a reorientation of the magnetic sublattices in Fe_2O_3 between 15 K and 300 K as predicted for a Morin transition. The saturation of the SMR amplitude at about 3 T with a slight decrease for higher field magnitudes due to canting effects, as described above, is observed at 15 K as well.

The explicit temperature dependence of the SMR amplitude at 7 T is shown in Fig. 5.11 (red symbols). In contrast to the resistance $\rho_{\mathrm{long}}(\alpha = 0°)$ of the Pt layer at $H = 7\,\mathrm{T}$ (black symbols), which increases monotonically from 15 K to 300 K as the expected temperature dependence for metallic Pt, the SMR amplitude is almost temperature independent. This result in AFM Pt|Fe_2O_3 bilayers is in contrast to the situation in Pt|YIG samples [38], where the SMR amplitude increases significantly with increasing temperature. This increase was attributed to the increase of the spin Hall angle in Pt from 0.075 at 10 K to 0.11 at room temperature [38]. Our new result here, however, calls this interpretation into question and needs further investigation. One possibility could be an increased canting of the sublattices with increasing temperature [47] which reduces the spin transfer torque at the interface and could compensate the effect of the increasing spin Hall angle.

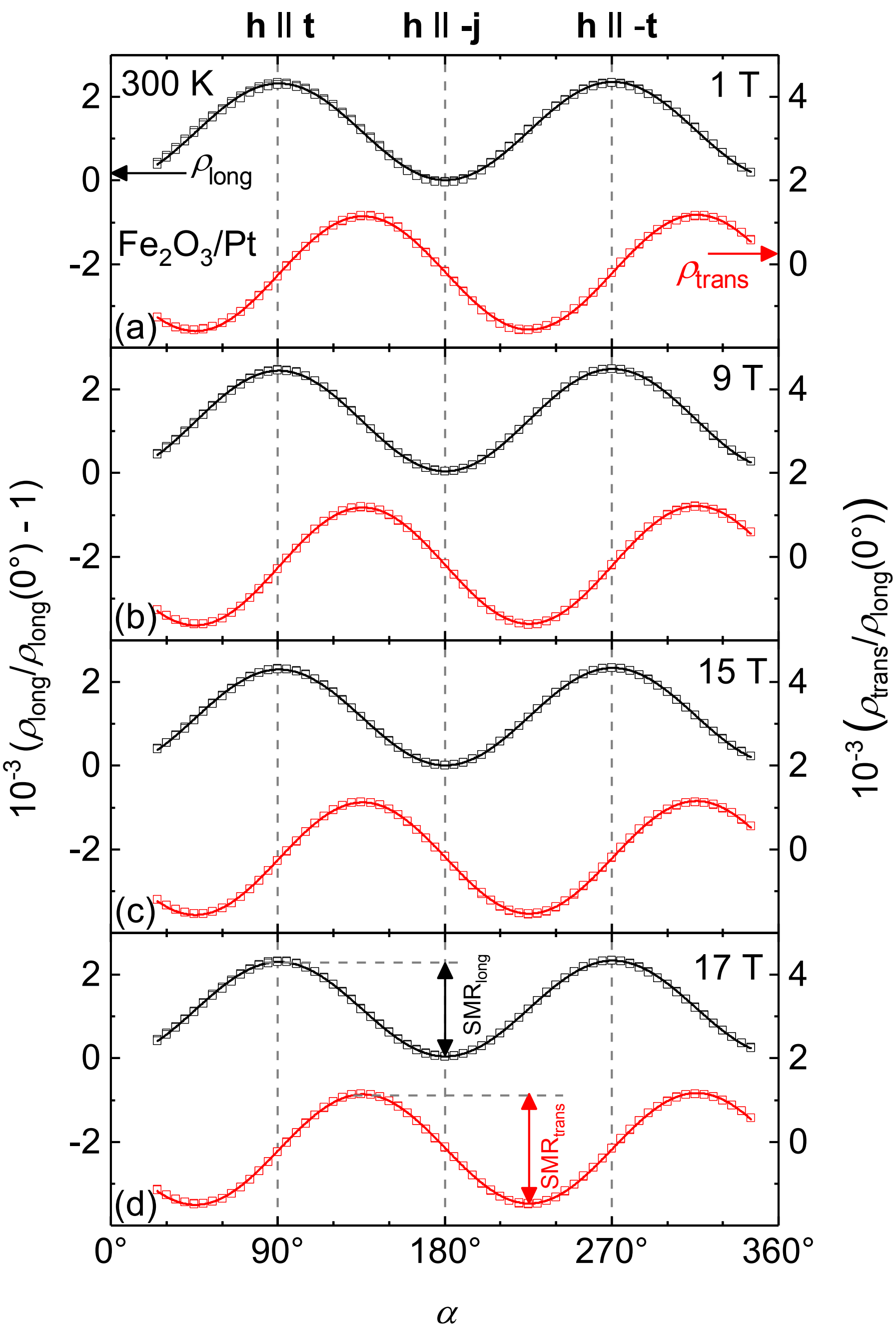

Figure 5.8: ADMR measurements of a $Fe_2O_3(0001)$/Pt bilayer, measured at 300 K at in-plane external magnetic field magnitudes of (a) 1 T, (b) 9 T, (c) 15 T, (d) 17 T. The normalized longitudinal resistivity ρ_{long} (black symbols, left axis) and transverse resistivity ρ_{trans} (red symbols, right axis) are shown as a function of the magnetic field orientation α. The lines are fits to the data according to Eqs. (4.4) and (4.5).

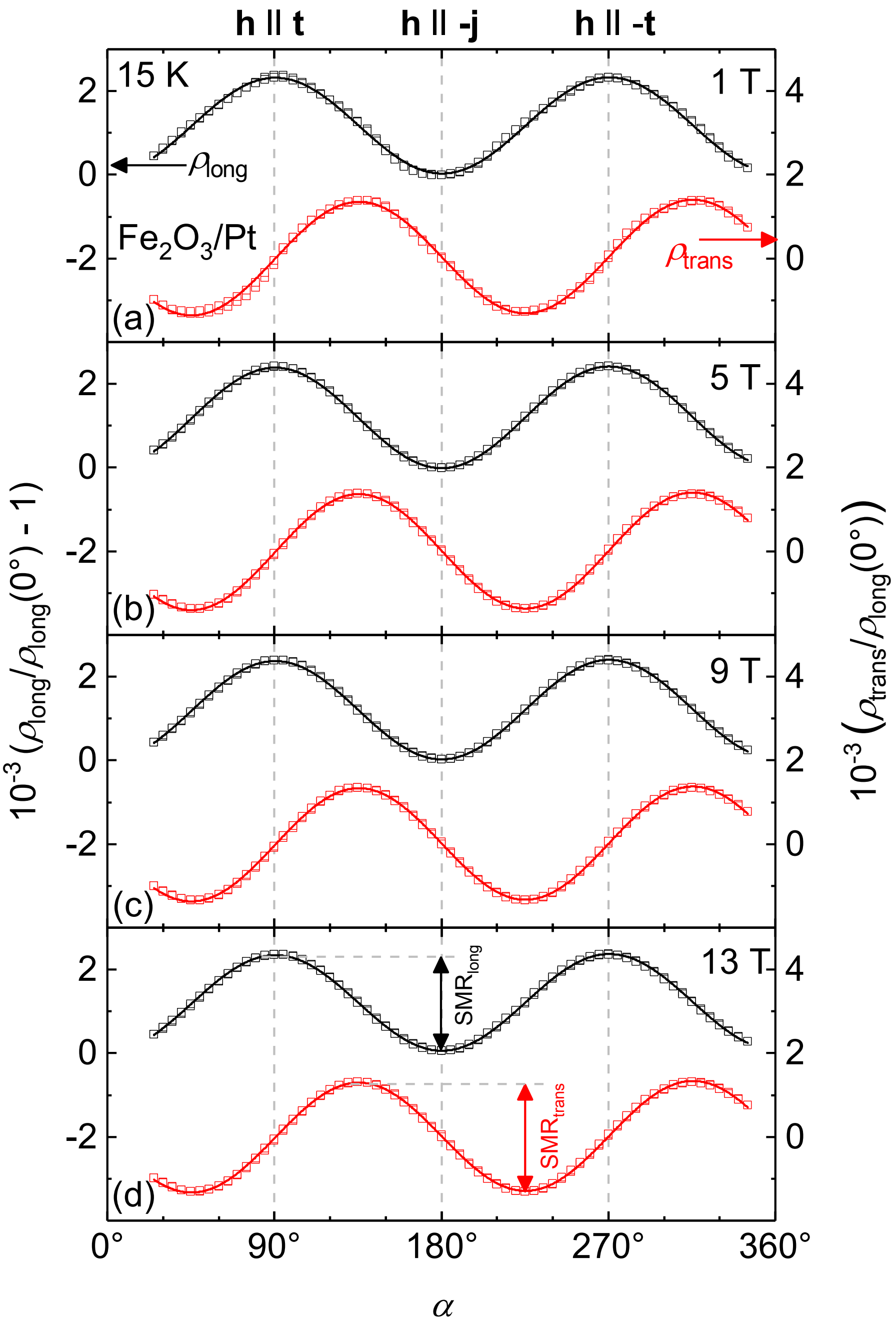

Figure 5.9: Low temperature ADMR measurements of a $Fe_2O_3(0001)$/Pt bilayer, measured at 15 K at in-plane external magnetic field magnitudes of (a) 1 T, (b) 5 T, (c) 9 T, (d) 13 T. The normalized longitudinal resistivity ρ_{long} (black symbols, left axis) and transverse resistivity ρ_{trans} (red symbols, right axis) are shown as a function of the magnetic field orientation α. The lines are fits to the data according to Eqs. (4.4) and (4.5).

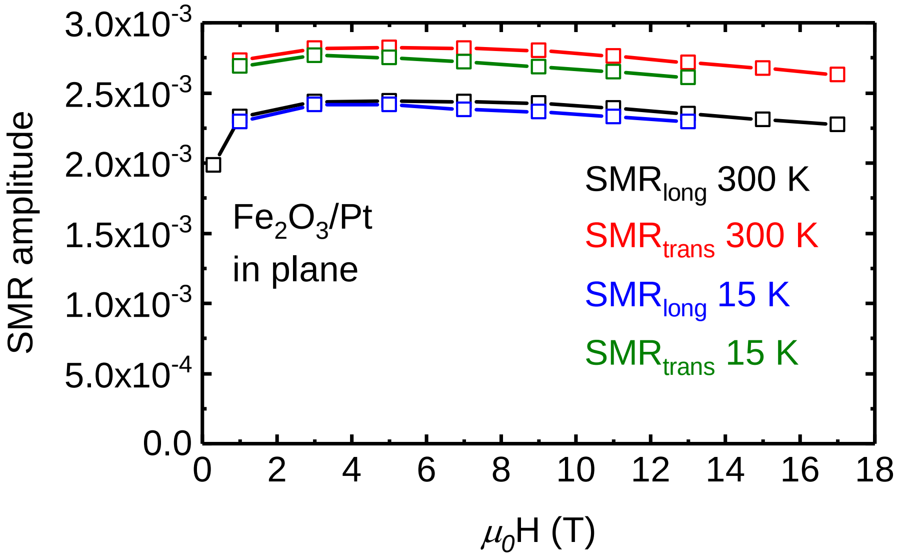

Figure 5.10: SMR amplitude of the $Fe_2O_3(0001)/Pt$ bilayer obtained from ADMR measurements at different external magnetic field magnitudes (cf. Figs. 5.7, 5.8, 5.9). The results from longitudinal (black and blue symbols) and transverse (red and green symbols) ADMR measurements are shown for 300 K and 15 K, respectively.

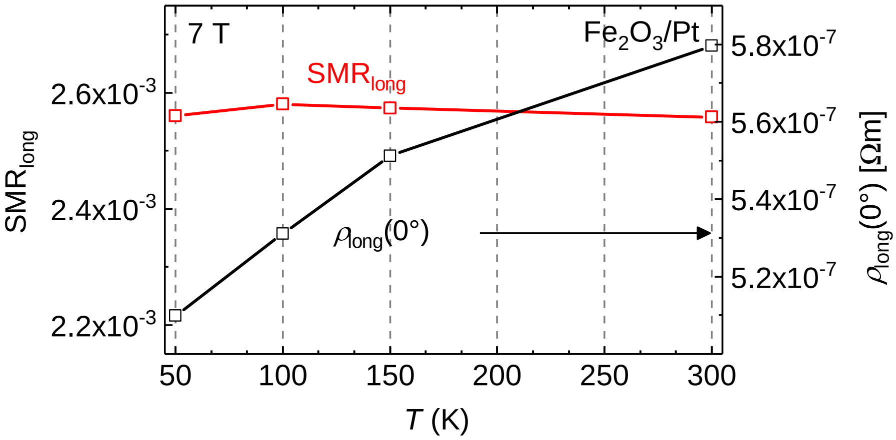

Figure 5.11: Temperature dependence of the longitudinal resistivity $\rho_{\text{long}}(\alpha = 0°)$ (black symbols), and the longitudinal SMR amplitude (red symbols). Both data sets are derived from ADMR measurements at an external field magnitude of 7 T.

5.3.3 Angle dependent MR for out-of-plane rotations of the external magnetic field H

Using the same definitions for the rotation planes as in chapter 4.3.2, we performed out-of-plane measurements of ρ_{long} in our Pt|$\mathrm{Fe_2O_3}$ samples at a constant field magnitude of 2 T (Fig. 5.12). Because of the small monodomain field, we could use a different measurement setup with a 3D vector magnet, where the ip and the two oop rotations can be carried out immediately one after each other without the need to remount the sample, and temperature instabilities are almost not visible (for details see Appendix). All data were normalized to the resistivity value at 0° where $\mathbf{h} \parallel \mathbf{j}$.

Again we find the coincidence of the oopt and the ip rotation at 0°, where $\mathbf{h} \parallel \mathbf{j}$ for both rotations. The oopj signal at 0° and the ip signal at 270° are also at the same resistivity level, because for both $\mathbf{h} \parallel -\mathbf{t}$. In contrast to NiO, the shape of the oop measurements in $\mathrm{Fe_2O_3}$ is different. From $\mathbf{h} \parallel \mathbf{j}$ ($\mathbf{h} \parallel -\mathbf{t}$) at 0° for oopt (oopj), the resistance levels stay constant at first, when we move towards $\mathbf{h} \parallel -\mathbf{n}$. Only in narrow regions around $\mathbf{h} \parallel \mathbf{n}, -\mathbf{n}$ the resistivities change to an intermediate level in between $\rho(\mathbf{h} \parallel \mathbf{t})$ and $\rho(\mathbf{h} \parallel \mathbf{j})$. As for NiO, we assign this case where the external field points out of the easy plane to an anisotropy dominated multidomain situation where the resistivity reaches $\rho_0 + \rho_1/2$. But as the energy scale differs from NiO, the curve of the oop data is different. In analogy to NiO, the SMR amplitude is represented by the difference of the oopj and the oopt signals at 0° and we find almost perfect agreement to the SMR amplitude of the ip rotation.

In summary, the SMR effect in the Pt|$\mathrm{Fe_2O_3}$ system can be described in the same framework of a three-domain model as the Pt|NiO system, but with a much smaller destressing energy resulting in a fast saturation of the SMR signal with increasing magnetic field.

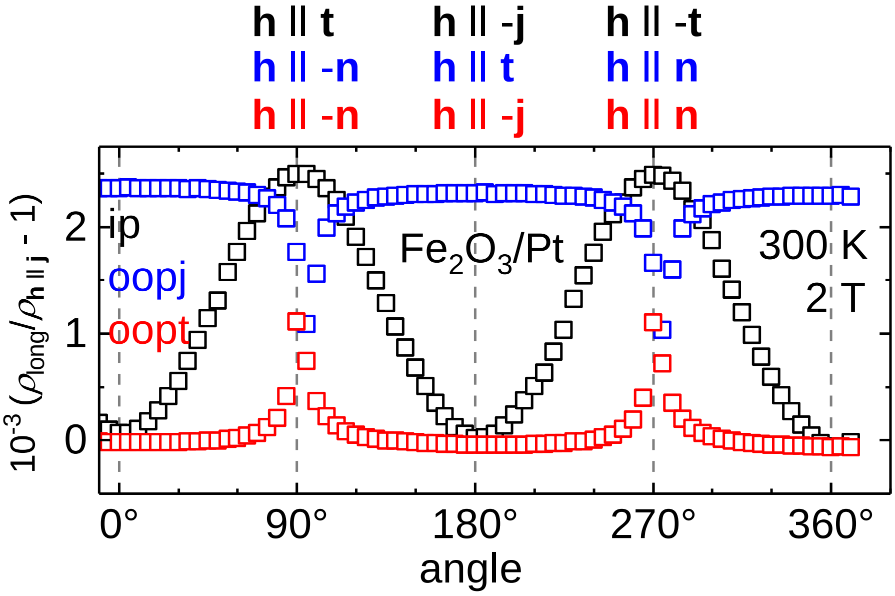

Figure 5.12: ADMR measurements of a $Fe_2O_3(0001)/Pt$ bilayer, measured at 300 K for out-of-plane (oop) external magnetic field rotations at 2 T. The longitudinal resistivities ρ_{long} for rotations around the **j** axis (oopj, blue symbols) and around the **t** axis (oopt, red symbols) are both normalized to the value $\rho_{\text{long}}(\mathbf{h}\|\mathbf{j})$ which corresponds to $\alpha = 0°$ in the ip rotation (black symbols), that is shown as a comparison.

Chapter 6

Summary and Outlook

6.1 Summary

We investigate the recently discovered spin Hall magnetoresistance (SMR) effect in bilayer thin film samples, using for the first time two different *antiferromagnetic* oxides (NiO and α-Fe_2O_3, respectively) covered with a Pt top electrode. We study the magnetoresistance while rotating a magnetic field of constant amplitude in or out of the film plane at different temperatures. For in-plane rotations, we find a 180° periodic oscillation of the longitudinal and the transverse resistivity, characteristic for the SMR effect, but shifted by 90° compared to the established results in ferrimagnetic insulator|Pt bilayers (i.e. $Y_3Fe_5O_{12}$(YIG)|Pt [31, 34]). In YIG|Pt the maximal SMR amplitude of 1.6×10^{-3} was already reached at 100 mT. In contrast the SMR amplitude in NiO|Pt shows an increase propotional to H^2 up to 12.5 T and saturates at 17 T with 7.8×10^{-4}. Similar to YIG|Pt, Fe_2O_3|Pt shows a fast saturation and reaches 2.5×10^{-3} at 3 T. Surprisingly, this value is higher than for YIG|Pt. Above 3 T, we even observe a slight decrease of the SMR amplitude. Measurements down to 15 K show the same results as for room temperature, indicating the absence of the controversally discussed Morin transition in our Fe_2O_3 thin films. Moreover we find an almost constant SMR amplitude over the whole temperature range in contrast to the observation in YIG|Pt [38]. For out-of-plane rotations we find the same longitudinal resistivity levels as for the in-plane rotation, where geometrically expected. When the external magnetic field vector points out of the film plane, the resistivity is at a value between the maximum and the minimum of the in-plane rotation. During the whole out-of-plane rotation the resistivity never gets higher or lower than for the ip-rotation.

To explain the in-plane observations at room temperature we developed a model for the SMR effect in antiferromagnetic insulator|Pt heterostructures [46]. In contrast to the single domain ferromagnet where the magnetization vector follows the external magnetic field [33], we consider a multidomain state with two antiferromagnetic sublattices per domain. The influence of an external field $\mathbf{H}$, rotating in the easy plane, first evokes a redistribution of the domain fractions, because domains with sublattice magnetizations perpendicular to $\mathbf{H}$ are energetically favourable. With increasing field magnitude we reach a monodomain state, where the sublattice magnetizations follow the rotation of the external field and orient always perpendicular to it. Formally we minimize the free energy as a sum of the anisotropy energy, the Zeeman energy and the so-called destressing energy [51–53] which can be seen as an analogon to the demagnetization energy in ferromagnets. As a result we obtain analytic expressions for the longitudinal and the transverse resistivity, shifted by 90° compared to the observations for ferrimagnet|Pt samples. The oscillation amplitude, i.e. the SMR signal, increases with H^2 and saturates at the monodomain field. The size of the monodomain field depends on the magnetostriction of the antiferromagnet.

The model represents a very good fit to our data and can be used to derive a value for the monodomain field. For NiO the monodomain field is at 13.4 T. For Fe_2O_3 the saturation of the SMR amplitude at low external field magnitudes makes it impossible to resolve the H^2 dependence in the experimental data. Therefore we can not name an exact value for a monodomain field, but nevertheless the data is in agreement to the model, assuming a low monodomain field. This assumption is reasonable because of the small magnetostriction in Fe_2O_3. We explain the decrease of the SMR amplitude at higher field magnitudes with canting effects. Furthermore the model can be used to explain the behaviour in bulk NiO|Pt [47] with a small monodomain field of 4.1 T [46].

6.2 Outlook

The results presented in this thesis provide a comprehensive picture of the in-plane SMR effect in NiO, where the experimental data are almost perfectly represented by the developed theoretical model. As we furthermore performed out-of-plane rotations an extention of the theory in this direction would be desirable. Besides we focused on measurements at room temperature, but low temperature experiments could complete the picture and explain the slight discrepancies between theory and experiment at the saturation of the SMR amplitude.

With the observation of the SMR in α-Fe_2O_3|Pt we found a second material to prove this effect in antiferromagnets. The higher SMR amplitude compared to NiO|Pt and YIG|Pt with its fast saturation for low external field magnitudes makes Fe_2O_3 a promising material for applications. To check the agreement to the theoretical model in detail, in particular the H^2 dependence of the SMR amplitude, measurements with a higher resolution up to the monodomain field are needed. To explain the decrease for even higher fields a more detailed theory, including canting effects, is desirable. Furthermore in this work we studied the SMR effect in Fe_2O_3|Pt down to low temperatures without detecting a remarkable change compared to room temperature. This temperature independence, as well as the absence of the Morin transition are subject to further investigation.

From the experimentalist's point of view, it is obvious to focus on other antiferromagnetic materials, i.e. on Cr_2O_3 or MnO, where the Néel temperature is experimentally accessible to cross-check the SMR scenario in antiferromagnets and complete the picture. In a future work one could moreover investigate the spin-Seebeck effect in the AFM|Pt samples. However, all these ideas are beyond the scope of this thesis.

Appendix A

Experimental Methods and Setups

In the first Part of the Appendix the experimental methods and setups used in this thesis will be discussed. These are pulsed laser deposition (PLD) and electron beam evaporation (EVAP) for the growth of thin film samples and X-ray diffraction (XRD) and magnetometry (SQUID) for their characterization. Then, the three setups used for magnetotransport measurements will be described. The second part contains a list of the growth parameters of the samples fabricated during this master's work. Some of the samples are discussed for this thesis.

A.1 Pulsed laser deposition (PLD)

The NiO and α-Fe_2O_3 thin films were grown on single crystalline Al_2O_3 and MgO substrates using PLD. As shown in Fig. A.1, pulses of a high energetic UV excimer laser (KrF, 248 nm, max. repetition rate 10 Hz) are focussed on a polycrystalline target (laser fluence 0.5 - 5 J/cm^2) to generate a plasma plume [77]. The ionized material accumulates on the single crystalline substrates that are heated by an infrared (IR) laser (140 W, 940 nm) from the backside to max. 1000 °C. The substrate temperature is measured via a pyrometer from outside the chamber. As we grow oxides, the samples are grown in an oxygen atmosphere under pressures between 10^{-4} and 1 mbar [77]. The growth is monitored by reflection high-energy electron diffraction (RHEED). By varying the growth parameters listed in Appendix B, we optimize the crystalline quality and obtain a highly epitaxial material at the desired thickness. PLD is a process far away from thermal equilibrium.

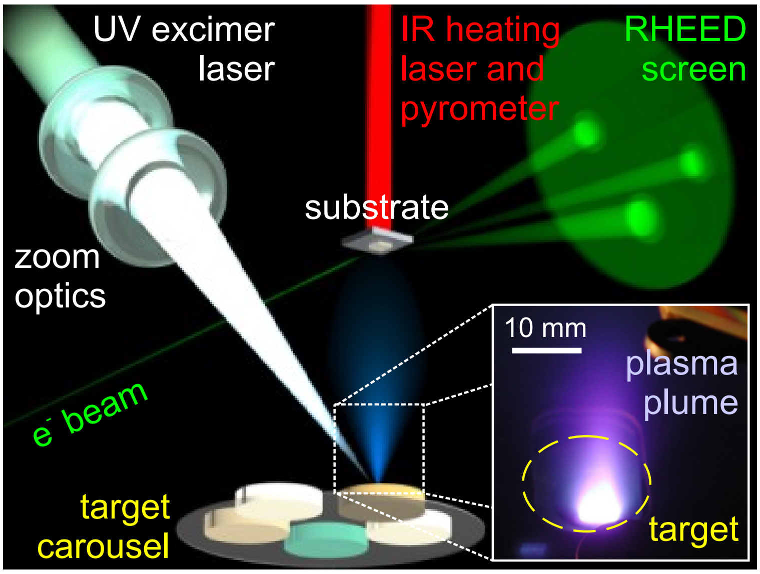

Figure A.1: Pulsed laser deposition (PLD) system at the Walther-Meissner-Institute. Figure taken from [65]

A.2 Electron beam evaporation (EVAP)

To deposit metallic electrodes in situ on top of the epitaxial antiferromagnet, we apply electron beam evaporation. There, the target material is heated thermally with an electron beam until its melting point. The electrons are generated by a filament, accelarated by an electric and focussed by a magnetic field. During the evaporation process, an oscillating crystal monitors the growth and permits to stop the process when the desired thickness is reached (see Fig. A.2).

A.3 X-ray diffractometry (XRD)

To characterize the samples and to determine their structural quality we employ X-ray diffraction. The X-rays with a wavelength of $\lambda = 0.154\,06\,\mathrm{nm}$ from the $\mathrm{Cu} - K_{\alpha 1}$ line are monochromatized by a Goebel mirror and a Ge(022) monochromator and subsequently diffracted from the sample. Due to constructive and destructive interference of the X-ray beam at the lattice planes, the diffraction angle Θ can be used to determine the distance between them (d_{hkl}) using Bagg's law:

$$n\lambda = 2d_{hkl}\sin\theta \ , \tag{A.1}$$

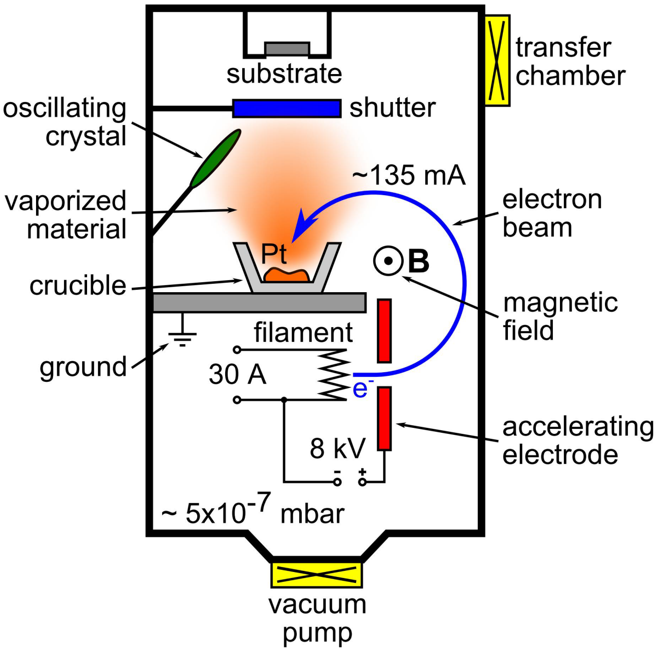

Figure A.2: Sketch of the used EVAP setup. Figure taken from Ref. [78].

When this equation is fulfilled we obtain constructive interference and get a maximum in the intensity. n indicates the order of the diffraction. To determine the out-of-plane lattice constant we carry out a single 2θ-ω-scan. There the sample is scanned with a constant 2θ-ω-relation (see Fig. A.3 for the angle definitions). For the in plane lattice constants, reciprocal space maps are recorded, consisting of several 2θ-ω-scans with differnt 2θ-ω-relations.

Depending on the crystalline structure we can use d_{hkl} to obtain the lattice constant a. For a cubic system, d_{hkl} is given by:

$$d_{hkl} = \frac{a}{\sqrt{h^2+k^2+l^2}} \; . \tag{A.2}$$

For a hexagonal sytem we use:

$$\frac{1}{d_{hkl}^2} = \left[\frac{4}{3}(h^2+k^2+hk) + l^2\left(\frac{a}{c}\right)^2\right]\frac{1}{a^2} \; . \tag{A.3}$$

h, k, l are the Miller indices for the three directions in reciprocal space.

To determine the thickness and the roughness of the layer stack, we use X-ray

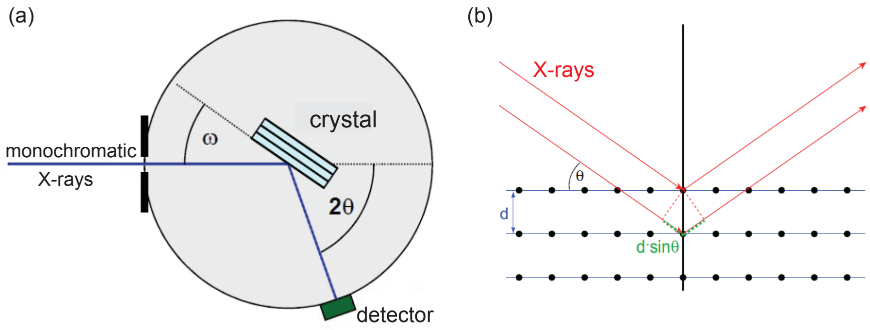

Figure A.3: Schematic picture of the X-ray beam path of the Bruker AXS D8 Discover system. Figure taken from Ref. [79].

reflectometry. This is a 2θ-ω scan with $0.5° < 2\theta < 5°$, so that the X-rays are diffracted at the surface and the interface instead of the lattice planes.

A.4 Superconducting quantum interference device (SQUID) magnetometry

To determine the magnetization of the thin films, we employ a superconducting quantum interference device (SQUID) magnetometer.

As shown in Fig. A.4(a), a sample glued with the diamagnetic “Marabu FIXOGUM” in a diamagnetic plastic straw is moved up and down a 2nd order gradiometer. This is the name of the measuring geometry of the superconducting pick-up coil to minimize the noise produced by interfering field gradients or fluctuations. As the straw passes all 4 loops it induces no signal, whereas the magnetic flux of the sample creates a current which is transformed by a RF-SQUID into a voltage curve (Fig. A.4(b)). So, the SQUID acts as an extremely sensitive flux-to-voltage converter.

The software fits the curve and determines the absolute magnetic moment m in the direction of the magnetic field. Then we have to subtract the signal of the substrate and determine the magnetization

$$M = \frac{m}{V} \tag{A.4}$$

of the sample by dividing by its volume V. We calculate V of the thin film by multiplying its thickness from X-ray reflectometry (Sec. A.3) with the surface area,

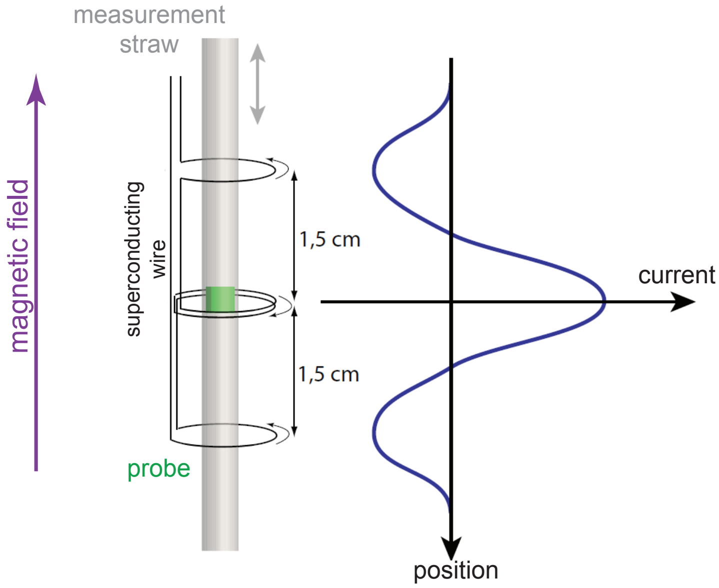

Figure A.4: Sketch of the gradiometer of the Squid magnetometer and the typically measured signal. Fig. taken from Ref. [80].

obtained from a microscope image.

We use a Quantum Design MPMS XL-7 magnetometer. Its superconducting magnet can create magnetic fields between -7 T and 7 T and the cooling system permits to vary the temperature between 1.8 K and 400 K.

A.5 Superconducting magnet cryostats

For the magnetotransport measurements in a wide temperature range we use three different cryogenic systems (Oxford Instruments) where the resistance can be determined as a function of the magnetic field magnitude, its direction, and the temperature. Each of the systems has its advantages. In a split coil magnet system we apply fields up to 7 T. Including remounting of the sample between each measurement, we carry out ip and oop measurements. A 3D vector magnet permits to do ip and oop measurements immediately without remounting, but only up to 2 T. Furthermore, we have a high field setup for ip measurements up to 17 T. All cryostats have a liquid He cooling system and can perform measurements between 2 K and 300 K. The temperature stability varies from system to system.

A.5.1 Split coil magnet system

We apply magnetic field magnitudes in horizontal direction up to 7 T. The dipstick is inserted vertically and can be rotated around its axis between −20° and 380°. The sample can be mounted with its surface horizontally or vertically and allows so ip and oop rotations, respectively. For NiO we measured the out-of-plane rotation (Fig. 4.12) with this system and for Fe_2O_3 the ip rotations at low field magnitudes (Fig. 5.7), as well as the temperature dependence of the SMR signal and the Pt resistivity (Fig. 5.11).

A.5.2 High field setup

In our high field cryostat, both the magnetic field and the sample surface are oriented vertically. On the dipstick a piezoelectric rotator (Attocube) rotates the sample in the plane of the magnetic field vector from 5° and 325°. All measurements up to high field magnitudes (i.e. Figs. 4.9, 4.10, 4.11, 5.8, 5.9) were carried out in this cryostat.

A.5.3 3D vector magnet system

Here, the sample rests and a with a 3D vector magnet the x-, y- and z-component of the magnetic field can be controlled separately. Even if this is not a real rotation, we can perform ip and oop angle dependent magnetoresistance measurements between −10° and 370°. The maximal field magnitudes in x- and y-direction are 2 T, in z-direction 7 T. As for Fe_2O_3 2 T are enough to obtain a monodomain state, we can use this system to compare the ip and the oop rotation without remounting the sample in between (Fig. 5.12).

Appendix B

Samples and parameters

All the individual fabrication conditions are summarized in this chapter.

Table B.1: Growth parameters and thicknesses of the NiO thin film samples and NiO|Pt bilayers fabricated on Al_2O_3 (0001) and MgO (111) substrates. The sample marked with an asterisk (*) is used for SMR measurements presented in this thesis.

Sample ID	Substrate	Energy (mJ)	Laser fluence (J/cm^2)	Temperature (°C)	O_2-Pressure (μbar)	Pulses	Repetition rate (Hz)	Thickness NiO|Pt (nm)
NIO14	Al_2O_3 (0001)	58.37	2.5	380	10	10 × 200	2	14.4 / 3.8
NIO15	Al_2O_3 (0001)	58.97	2.5	380	10	60 × 200	2	80.9 / 3.6
NIO17	Al_2O_3 (0001)	57.69	2.5	380	10	90 × 200	2	91.6 / 3.2
NIO21*	Al_2O_3 (0001)	58.82	2.5	380	10	90 × 200	2	120.0 / 5.0
NIO16	MgO (111)	58.09	2.5	380	10	60 × 200	2	74.0 / 3.1
NIO18	MgO (111)	56.22	2.5	380	10	90 × 200	2	111.8 /3.0

Table B.2: Growth parameters and thicknesses of the Fe_2O_3 thin film samples and Fe_2O_3 |Pt bilayers fabricated on Al_2O_3 (0001) and (11-20). The sample marked with an asterisk (*) is used for SMR measurements presented in this thesis.

Sample ID	Substrate	Energy (mJ)	Laser fluence (J/cm^2)	Temperature (°C)	O_2-Pressure (μbar)	Pulses	Repetition rate (Hz)	Thickness Fe_2O_3 |Pt (nm)
FEOS4	Al_2O_3 (0001)	52.73	2.5	320	25	66 × 300	2	41.2 / 2.1
FEOS5	Al_2O_3 (0001)	59.06	2.5	320	25	66 × 300	2	69.9 / 1.8
FEOS9	Al_2O_3 (0001)	58.05	2.5	320	25	132 × 300	2	– / –
FEOS11*	Al_2O_3 (0001)	54.92	2.5	320	25	132 × 300	2	90.0 / 3.0
FEOS12	Al_2O_3 (0001)	55.61	2.5	320	50	132 × 300	2	– / –
FEOS6	Al_2O_3 $(11\bar{2}0)$	58.51	2.5	320	25	66 × 300	2	61.4 / 1.8
FEOS7	Al_2O_3 $(11\bar{2}0)$	58.32	2.5	320	25	66 × 300	2	81.1 / 2.1
FEOS8	Al_2O_3 $(11\bar{2}0)$	57.51	2.5	320	25	132 × 300	2	– / –

Bibliography

[1] A. S. Núñez, R. A. Duine, P. Haney, and A. H. MacDonald, "Theory of spin torques and giant magnetoresistance in antiferromagnetic metals", Phys. Rev. B **73**, 214426 (2006).

[2] A. B. Shick, S. Khmelevskyi, O. N. Mryasov, J. Wunderlich, and T. Jungwirth, "Spin-orbit coupling induced anisotropy effects in bimetallic antiferromagnets: A route towards antiferromagnetic spintronics", Phys. Rev. B **81**, 212409 (2010).

[3] A. H. MacDonald and M. Tsoi, "Antiferromagnetic metal spintronics", Philosophical Transactions of the Royal Society of London A: Mathematical, Physical and Engineering Sciences **369**, 3098 (2011).

[4] V. M. T. S. Barthem, C. V. Colin, H. Mayaffre, M.-H. Julien, and D. Givord, "Revealing the properties of Mn_2Au for antiferromagnetic spintronics", Nature Communications **4**, 2892 (2013).

[5] E. V. Gomonay and V. M. Loktev, "Spintronics of antiferromagnetic systems (Review Article)", Low Temperature Physics **40**, 17 (2014).

[6] R. Macêdo and T. Dumelow, "Tunable all-angle negative refraction using antiferromagnets", Phys. Rev. B **89**, 035135 (2014).

[7] J. Železný, H. Gao, K. Výborný, J. Zemen, J. Mašek, A. Manchon, J. Wunderlich, J. Sinova, and T. Jungwirth, "Relativistic Néel-Order Fields Induced by Electrical Current in Antiferromagnets", Phys. Rev. Lett. **113**, 157201 (2014).

[8] R. Cheng, J. Xiao, Q. Niu, and A. Brataas, "Spin Pumping and Spin-Transfer Torques in Antiferromagnets", Phys. Rev. Lett. **113**, 057601 (2014).

[9] V. Tshitoyan, C. Ciccarelli, A. P. Mihai, M. Ali, A. C. Irvine, T. A. Moore, T. Jungwirth, and A. J. Ferguson, "Electrical manipulation of ferromagnetic NiFe by antiferromagnetic IrMn", Phys. Rev. B **92**, 214406 (2015).

[10] T. Jungwirth, X. Marti, P. Wadley, and J. Wunderlich, "Antiferromagnetic spintronics", Nature Nanotechnology **11**, 231 (2016).

[11] V. Baltz, A. Manchon, M. Tsoi, T. Moriyama, T. Ono, and Y. Tserkovnyak, arXiv:1606.04284 [Rev. Mod. Phys. (2017) (accepted)].

[12] T. Satoh, R. Iida, T. Higuchi, M. Fiebig, and T. Shimura, "Writing and reading of an arbitrary optical polarization state in an antiferromagnet", Nature Photonics **9**, 2 (2014).

[13] X. Marti, I. Fina, C. Frontera, J. Liu, P. Wadley, Q. He, R. J. Paull, J. D. Clarkson, J. Kudrnovský, I. Turek, J. Kuneš, D. Yi, J.-H. Chu, C. T. Nelson, L. You, E. Arenholz, S. Salahuddin, J. Fontcuberta, T. Jungwirth, and R. Ramesh, "Room-temperature antiferromagnetic memory resistor", Nature Materials **13**, 367 (2014).

[14] P. Wadley, B. Howells, J. Železný, C. Andrews, V. Hills, R. P. Campion, V. Novák, K. Olejník, F. Maccherozzi, S. S. Dhesi, S. Y. Martin, T. Wagner, J. Wunderlich, F. Freimuth, Y. Mokrousov, J. Kuneš, J. S. Chauhan, M. J. Grzybowski, A. W. Rushforth, K. W. Edmonds, B. L. Gallagher, and T. Jungwirth, "Electrical switching of an antiferromagnet", Science **351**, 587 (2016).

[15] H. Chen, Q. Niu, and A. H. MacDonald, "Anomalous Hall Effect Arising from Noncollinear Antiferromagnetism", Phys. Rev. Lett. **112**, 017205 (2014).

[16] J. B. S. Mendes, R. O. Cunha, O. Alves Santos, P. R. T. Ribeiro, F. L. A. Machado, R. L. Rodríguez-Suárez, A. Azevedo, and S. M. Rezende, "Large inverse spin Hall effect in the antiferromagnetic metal $Ir_{20}Mn_{80}$", Phys. Rev. B **89**, 140406 (2014).

[17] W. Zhang, M. B. Jungfleisch, W. Jiang, J. E. Pearson, A. Hoffmann, F. Freimuth, and Y. Mokrousov, "Spin Hall Effects in Metallic Antiferromagnets", Phys. Rev. Lett. **113**, 196602 (2014).

[18] Y. Ou, S. Shi, D. C. Ralph, and R. A. Buhrman, "Strong spin Hall effect in the antiferromagnet PtMn", Phys. Rev. B **93**, 220405 (2016).

[19] Y. Ohnuma, H. Adachi, E. Saitoh, and S. Maekawa, “Spin Seebeck effect in antiferromagnets and compensated ferrimagnets”, Phys. Rev. B **87**, 014423 (2013).

[20] S. Seki, T. Ideue, M. Kubota, Y. Kozuka, R. Takagi, M. Nakamura, Y. Kaneko, M. Kawasaki, and Y. Tokura, “Thermal Generation of Spin Current in an Antiferromagnet”, Phys. Rev. Lett. **115**, 266601 (2015).

[21] S. M. Wu, W. Zhang, K. Amit, P. Borisov, J. E. Pearson, J. S. Jiang, D. Lederman, A. Hoffmann, and A. Bhattacharya, “Antiferromagnetic Spin Seebeck Effect”, Phys. Rev. Lett. **116**, 097204 (2016).

[22] S. M. Rezende, R. L. Rodríguez-Suárez, and A. Azevedo, “Theory of the spin Seebeck effect in antiferromagnets”, Phys. Rev. B **93**, 014425 (2016).

[23] R. Cheng, S. Okamoto, and D. Xiao, “Spin Nernst Effect of Magnons in Collinear Antiferromagnets”, Phys. Rev. Lett. **117**, 217202 (2016).

[24] P. Merodio, A. Ghosh, C. Lemonias, E. Gautier, U. Ebels, M. Chshiev, H. Béa, V. Baltz, and W. E. Bailey, “Penetration depth and absorption mechanisms of spin currents in $Ir_{20}Mn_{80}$ and $Fe_{50}Mn_{50}$ polycrystalline films by ferromagnetic resonance and spin pumping”, Applied Physics Letters **104**, 032406 (2014).

[25] H. Wang, C. Du, P. C. Hammel, and F. Yang, “Antiferromagnonic Spin Transport from $Y_3Fe_5O_{12}$ into NiO”, Phys. Rev. Lett. **113**, 097202 (2014).

[26] C. Hahn, G. de Loubens, V. V. Naletov, J. B. Youssef, O. Klein, and M. Viret, “Conduction of spin currents through insulating antiferromagnetic oxides”, EPL (Europhysics Letters) **108**, 57005 (2014).

[27] H. Wang, C. Du, P. C. Hammel, and F. Yang, “Spin transport in antiferromagnetic insulators mediated by magnetic correlations”, Phys. Rev. B **91**, 220410 (2015).

[28] T. Moriyama, S. Takei, M. Nagata, Y. Yoshimura, N. Matsuzaki, T. Terashima, Y. Tserkovnyak, and T. Ono, “Anti-damping spin transfer torque through epitaxial nickel oxide”, Applied Physics Letters **106**, 162406 (2015).

[29] W. Lin, K. Chen, S. Zhang, and C. L. Chien, “Enhancement of Thermally Injected Spin Current through an Antiferromagnetic Insulator”, Phys. Rev. Lett. **116**, 186601 (2016).

[30] T. Shang, Q. F. Zhan, H. L. Yang, Z. H. Zuo, Y. L. Xie, L. P. Liu, S. L. Zhang, Y. Zhang, H. H. Li, B. M. Wang, Y. H. Wu, S. Zhang, and R.-W. Li, "Effect of NiO inserted layer on spin-Hall magnetoresistance in Pt/NiO/YIG heterostructures", Applied Physics Letters **109**, 032410 (2016).

[31] H. Nakayama, M. Althammer, Y.-T. Chen, K. Uchida, Y. Kajiwara, D. Kikuchi, T. Ohtani, S. Geprägs, M. Opel, S. Takahashi, R. Gross, G. E. W. Bauer, S. T. B. Goennenwein, and E. Saitoh, "Spin Hall Magnetoresistance Induced by a Nonequilibrium Proximity Effect", Phys. Rev. Lett. **110**, 206601 (2013).

[32] J. E. Hirsch, "Spin Hall Effect", Phys. Rev. Lett. **83**, 1834 (1999).

[33] Y.-T. Chen, S. Takahashi, H. Nakayama, M. Althammer, S. T. B. Goennenwein, E. Saitoh, and G. E. W. Bauer, "Theory of spin Hall magnetoresistance", Phys. Rev. B **87**, 144411 (2013).

[34] M. Althammer, S. Meyer, H. Nakayama, M. Schreier, S. Altmannshofer, M. Weiler, H. Huebl, S. Geprägs, M. Opel, R. Gross, D. Meier, C. Klewe, T. Kuschel, J.-M. Schmalhorst, G. Reiss, L. Shen, A. Gupta, Y.-T. Chen, G. E. W. Bauer, E. Saitoh, and S. T. B. Goennenwein, "Quantitative study of the spin Hall magnetoresistance in ferromagnetic insulator/normal metal hybrids", Phys. Rev. B **87**, 224401 (2013).

[35] N. Vlietstra, J. Shan, V. Castel, B. J. van Wees, and J. Ben Youssef, "Spin-Hall magnetoresistance in platinum on yttrium iron garnet: Dependence on platinum thickness and in-plane/out-of-plane magnetization", Phys. Rev. B **87**, 184421 (2013).

[36] C. Hahn, G. de Loubens, O. Klein, M. Viret, V. V. Naletov, and J. Ben Youssef, "Comparative measurements of inverse spin Hall effects and magnetoresistance in YIG/Pt and YIG/Ta", Phys. Rev. B **87**, 174417 (2013).

[37] S. R. Marmion, M. Ali, M. McLaren, D. A. Williams, and B. J. Hickey, "Temperature dependence of spin Hall magnetoresistance in thin YIG/Pt films", Phys. Rev. B **89**, 220404 (2014).

[38] S. Meyer, M. Althammer, S. Geprägs, M. Opel, R. Gross, and S. T. B. Goennenwein, "Temperature dependent spin transport properties of platinum inferred

from spin Hall magnetoresistance measurements", Applied Physics Letters **104**, 242411 (2014).

[39] M. Aldosary, J. Li, C. Tang, Y. Xu, J.-G. Zheng, K. N. Bozhilov, and J. Shi, "Platinum/yttrium iron garnet inverted structures for spin current transport", Applied Physics Letters **108**, 242401 (2016).

[40] M. Isasa, A. Bedoya-Pinto, S. Vélez, F. Golmar, F. Sánchez, L. E. Hueso, J. Fontcuberta, and F. Casanova, "Spin Hall magnetoresistance at Pt/$CoFe_2O_4$ interfaces and texture effects", Applied Physics Letters **105**, 142402 (2014).

[41] K. Ganzhorn, J. Barker, R. Schlitz, B. A. Piot, K. Ollefs, F. Guillou, F. Wilhelm, A. Rogalev, M. Opel, M. Althammer, S. Geprägs, H. Huebl, R. Gross, G. E. W. Bauer, and S. T. B. Goennenwein, "Spin Hall magnetoresistance in a canted ferrimagnet", Phys. Rev. B **94**, 094401 (2016).

[42] A. Aqeel, N. Vlietstra, A. Roy, M. Mostovoy, B. J. van Wees, and T. T. M. Palstra, "Electrical detection of spiral spin structures in Pt|Cu_2OSeO_3 heterostructures", Phys. Rev. B **94**, 134418 (2016).

[43] W. Lin and C. L. Chien, "Electrical Detection of Spin Backflow from an Antiferromagnetic Insulator/$Y_3Fe_5O_{12}$ Interface", Phys. Rev. Lett. **118**, 067202 (2017).

[44] Y.-M. Hung, C. Hahn, H. Chang, M. Wu, H. Ohldag, and A. D. Kent, "Spin transport in antiferromagnetic NiO and magnetoresistance in $Y_3Fe_5O_{12}$/NiO/Pt structures", AIP Advances **7**, 055903 (2017).

[45] D. Hou, Z. Qiu, J. Barker, K. Sato, K. Yamamoto, S. Vélez, J. M. Gomez-Perez, L. E. Hueso, F. Casanova, and E. Saitoh, "Tunable Sign Change of Spin Hall Magnetoresistance in Pt/NiO/YIG Structures", Phys. Rev. Lett. **118**, 147202 (2017).

[46] J. Fischer, S. Geprägs, R. Schlitz, K. Ganzhorn, N. Vlietstra, O. Gomonay, M. Althammer, H. Huebl, M. Opel, R. Gross, and S. T. B. Goennenwein, "Spin Hall magnetoresistance in antiferromagnet/normal metal heterostructures", (2017), to be submitted.

[47] G. R. Hoogeboom, A. Aqeel, T. Kuschel, T. T. M. Palstra, and B. J. van Wees, "Negative spin Hall magnetoresistance of Pt on the bulk easy-plane antiferromagnet NiO", Applied Physics Letters **111**, 052409 (2017).

[48] A. N. Bogdanov, A. V. Zhuravlev, and U. K. Rößler, "Spin-flop transition in uniaxial antiferromagnets: Magnetic phases, reorientation effects, and multidomain states", Phys. Rev. B **75**, 094425 (2007).

[49] L. Néel, "Antiferromagnetism and Ferrimagnetism", The Proceedings of the Physical Society of London Section A **65**, 57 (1952).

[50] E. Uchida, N. Fukuoka, H. Kondoh, T. Takeda, Y. Nakazumi, and T. Nagamiya, "Magnetic Anisotropy of Single Crystals of NiO and MnO", Journal of the Physical Society of Japan **23**, 1197 (1967).

[51] E. V. Gomonay and V. M. Loktev, "Theory of magnetoresistance anisotropy in the lamellar underdoped copper oxides", Phys. Rev. B **64**, 064406 (2001).

[52] H. Gomonay and V. M. Loktev, "Magnetostriction and magnetoelastic domains in antiferromagnets", Journal of Physics: Condensed Matter **14**, 3959 (2002).

[53] H. V. Gomonay and V. M. Loktev, "Shape-induced phenomena in finite-size antiferromagnets", Phys. Rev. B **75**, 174439 (2007).

[54] G. Srinivasan and M. S. Seehra, "Magnetic susceptibilities, their temperature variation, and exchange constants of NiO", Phys. Rev. B **29**, 6295 (1984).

[55] W. L. Roth, "Magnetic Structures of MnO, FeO, CoO, and NiO", Phys. Rev. **110**, 1333 (1958).

[56] M. T. Hutchings and E. J. Samuelsen, "Measurement of Spin-Wave Dispersion in NiO by Inelastic Neutron Scattering and Its Relation to Magnetic Properties", Phys. Rev. B **6**, 3447 (1972).

[57] F. L. A. Machado, P. R. T. Ribeiro, J. Holanda, R. L. Rodríguez-Suárez, A. Azevedo, and S. M. Rezende, "Spin-flop transition in the easy-plane antiferromagnet nickel oxide", Phys. Rev. B **95**, 104418 (2017).

[58] H. P. Rooksby, "A note on the structure of nickel oxide at subnormal and elevated temperatures", Acta Crystallogr. **1**, 226 (1948).

[59] W. L. Roth, “Neutron and Optical Studies of Domains in NiO”, Journal of Applied Physics **31**, 2000 (1960).

[60] T. Yamada, S. Saito, and Y. Shimomura, “Magnetic Anisotropy, Magnetostriction, and Magnetic Domain Walls in NiO. II. Experiment”, Journal of the Physical Society of Japan **21**, 672 (1966).

[61] P. de V Du Plessis, S. J. van Tonder, and L. Alberts, “Elastic constants of a NiO single crystal: I (Magnetic transitions)”, Journal of Physics C: Solid State Physics **4**, 1983 (1971).

[62] P. de V Du Plessis, S. J. van Tonder, and L. Alberts, “Magnetostriction of a NiO single crystal II”, Journal of Physics C: Solid State Physics **4**, 2565 (1971).

[63] A. Nielsen, A. Brandlmaier, M. Althammer, W. Kaiser, M. Opel, J. Simon, W. Mader, S. T. B. Goennenwein, and R. Gross, “All oxide ferromagnet/semiconductor epitaxial heterostructures”, Applied Physics Letters **93**, 162510 (2008).

[64] M. Opel, S. Geprägs, E. P. Menzel, A. Nielsen, D. Reisinger, K.-W. Nielsen, A. Brandlmaier, F. D. Czeschka, M. Althammer, M. Weiler, S. T. B. Goennenwein, J. Simon, M. Svete, W. Yu, S.-M. Hühne, W. Mader, and R. Gross, “Novel multifunctional materials based on oxide thin films and artificial heteroepitaxial multilayers”, physica status solidi (a) **208**, 232 (2011).

[65] M. Opel, “Spintronic oxides grown by laser-MBE”, Journal of Physics D: Applied Physics **45**, 033001 (2012).

[66] J. W. Arblaster, “Crystallographic Properties of Platinum”, Platinum Metals Review **41**, 12 (1997).

[67] D. C. Giancoli, *Physics* (Prentice Hall, 1995).

[68] M. Lübbe, “Präparation und magnetische Eigenschaften dünner Fe_2O_3- und $FeTi_{1-x}O_3$-Schichten auf Al_2O_3(0001)”, Phd thesis, Ludwig-Maximilians-Universität München (2009), URL `http://nbn-resolving.de/urn:nbn:de:bvb:19-102517`.

[69] N. Shimomura, S. Pati, Y. Sato, T. Nozaki, T. Shibata, K. Mibu, and M. Sahashi, “Morin transition temperature in (0001)-oriented α-Fe_2O_3 thin film and effect of Ir doping”, Journal of Applied Physics **117**, 17C736 (2015).

[70] T. Fujii, M. Takano, R. Kakano, Y. Isozumi, and Y. Bando, “Spin-flip anomalies in epitaxial $\alpha-Fe_2O_3$ films by Moessbauer spectroscopy”, Journal of Magnetism and Magnetic Materials **135**, 231 (1993).

[71] S. Gota, M. Gautier-Soyer, and M. Sacchi, “Magnetic properties of Fe_2O_3(0001) thin layers studied by soft x-ray linear dichroism”, Phys. Rev. B **64**, 224407 (2001).

[72] J. Dho, C. W. Leung, Z. H. Barber, and M. G. Blamire, “Controlling the exchange interaction using the spin-flip transition of antiferromagnetic spins in $Ni_{81}Fe_{19}/\alpha$-Fe_2O_3”, Journal of Applied Physics **97**, 10K101 (2005).

[73] S. Park, H. Jang, J.-Y. Kim, B.-G. Park, T.-Y. Koo, and J.-H. Park, “Strain control of Morin temperature in epitaxial α-Fe 2 O 3 (0001) film”, EPL (Europhysics Letters) **103**, 27007 (2013).

[74] F. J. Morin, “Electrical Properties of α-Fe_2O_3 and α-Fe_2O_3 Containing Titanium”, Phys. Rev. **83**, 1005 (1951).

[75] R. A. Voskanyan, R. Z. Levitin, and V. A. Shchurov, “Magnetostriction of a hematite monocrystal in fields up to 150 kOe”, Soviet. Phys. JETP **27**, 423 (1968).

[76] J. C. Marmeggi, D. Hohlwein, and E. F. Bertaut, “Magnetic neutron laue diffraction study of the domain distribution in α-Fe2O3”, physica status solidi (a) **39**, 57 (1977).

[77] M. Opel, S. Geprägs, M. Althammer, T. Brenninger, and R. Gross, “Laser molecular beam epitaxy of ZnO thin films and heterostructures”, Journal of Physics D: Applied Physics **47**, 034002 (2014).

[78] F. Schade, “Fabrication and Characterization of $Y_3Fe_5O_{12}|Pt|Y_3Fe_5O_{12}$ Trilayers for Spin Current Based Experiments”, Bachelor thesis, Technische Universität München (2013).

[79] U. Pietsch, V. Holy, and T. Baumbach, *High-Resolution X-Ray Scattering* (Springer, 1999).

[80] K. W. Nielsen, “Ursache der magnetischen Kopplung in Kobalt-dotiertem ZnO”, Ph.D. thesis, Technische Universität München (2007).

Acknowledgement

To the end, I would like to thank all the people involved in this thesis, in particular:

- Prof. Dr. Rudolf Gross for the opportunity to continue working at the Walther-Meissner-Institute for my Master's thesis in the magnetism group, after I wrote the Bachelor's thesis in the Qubit group. You gave me the possibility to join several workshops (summer school on oxide electronics in Cargèse, DPG spring meeting in Dresden, SPICE workshop in Mainz) to broaden my horizon in the area of oxide electronics and to get in touch with some experts in the field. Besides, the uncomplicated way of organizing my colloquium enabled me to finish my Master's degree in time to start a PhD at the Unité Mixte CNRS/Thales. I also thank you for the letter of recommendation required for the graduate school there.

- Dr. Matthias Opel for the best possible support for my Master's thesis. Beginning with the very good and patient advice in the lab, that allowed me to understand the concepts of the measurements as well as the interpretation of the results in the physical context. You always took a lot of time to answer all my numerous endless questions on physics and believed in my capacity to understand even complex subjects. You helped me to stay motivated and not to give up, even though sometimes my calculations, for example, made me a bit desperate. And, of course, for three times proof-reading this thesis, which included lots of constructive ideas and represented an enourmous help to structure and finish it.

- Dr. Stephan Geprägs for the kind instruction to various laboratory equipment, helpful explanations and discussions during the whole Master's thesis. In spite of your enourmous workload, where I nearly felt sorry to ask, you never said 'no' and always helped me immediately with whatever problem came up.

- Prof. Dr. Olena Gomonay for the great theory support to explain our experimental data to the SMR in NiO|Pt, for careful proof-reading of Chapter 3 and your quick response to all further questions.

- Dr. Matthias Althammer for your open ear and help with all my questions concerning lab issues and data analysis. And thank you very much for various Adobe Illustrator Figure templates, which I could modify for this thesis.

- Dr. Nynke Vlietstra for motivating discussions leading for example to Fig. 2.3, as well as some hours of soldering to get the Attocube rotator working in the cryostat at 17 T.

- Kathrin Ganzhorn for the introduction into the SMR data analysis and all the correspondence with Attocube including various repairs of the rotator.

- Tobias Wimmer for your kind introduction to the Chaos-3D-vector magnet system.

- Dr. Hans Hübl for a fruitful discussion-'Gelage' in our master's office and for motivating me to productive writing to finish my thesis in time.

- Prof. Dr. Andreas Erb for the introduction to Laue imaging and determining the orientation of my substrates.

- Karen Helm-Knapp and Astrid Habel for your patience with me and the circular diamond saw when cutting the substrates.

- Christoph Kastl for a kind instruction how to solder the contacts of the breakout box.

- Thomas Brenninger for continuous technical support on a very fast time scale concerning all issues in thin film technology.

- Technical staff of the Walther-Meissner-Institute, especially Helmut Thies and his team for taking care of the experimental equipment.

- All the people I shared an office with (Michaela Schleuder, Sebastian Oberauer, Lukas Liensberger, Christian Besson, Jan-Robin Scholz) including Sarah Gelder for creating such a friendly and 'productive' working environment and helping me with whatever came up concerning computer bugs or lab issues.

- All members of the magnetism group for fruitful discussions in three group meetings per week and the productive working atmosphere.
- Prof. Dr. Sebastian T.B. Gönnenwein for the initial idea to study the SMR in NiO|Pt bilayers.
- Prof. Dr. Christian Pfleiderer for the kind organization of the colloquium and for still being as friendly as ten years ago, when I was in your group for the motivating 'Schülerpraktikum'.
- Dr. Kirill Fedorov for your interest in my work even though I changed subject after the Bachelor thesis, which I still remember as a great, funny time with the cooling-box. And thank you very much for the letter of recommendation for the application at the graduate school.
- Dr. Manuel Bibes and your group in France for a six month internship at the Unité Mixte CNRS/Thales, including the invitation to the summer school on oxide electronics and my first DPG spring meeting in 2016, which gave me some experience in science before starting my Master's thesis in Germany. And I thank you for all the necessary organisation in advance which gives me the possibility to proceed with the PhD in your group to continue my research in the field of oxide electronics.
- Prof. Dr. B.S. Chandrasekhar for being an exemplary physicist who is still curious about new experimental developements and many other things like music. Thank you very much for your interest in my orchestra concerts as well as the impressing visit to the Semperoper in Dresden.
- Last but not least I want to thank my family and my friends for always supporting me and my work, even if I sometimes stayed in the lab until late at night or returned home in a bad mood, because the results of the experiments or calculations affected me so directly.

I gratefully acknowledge financial support by the Deutschlandstipendium during the year of the Master's thesis.